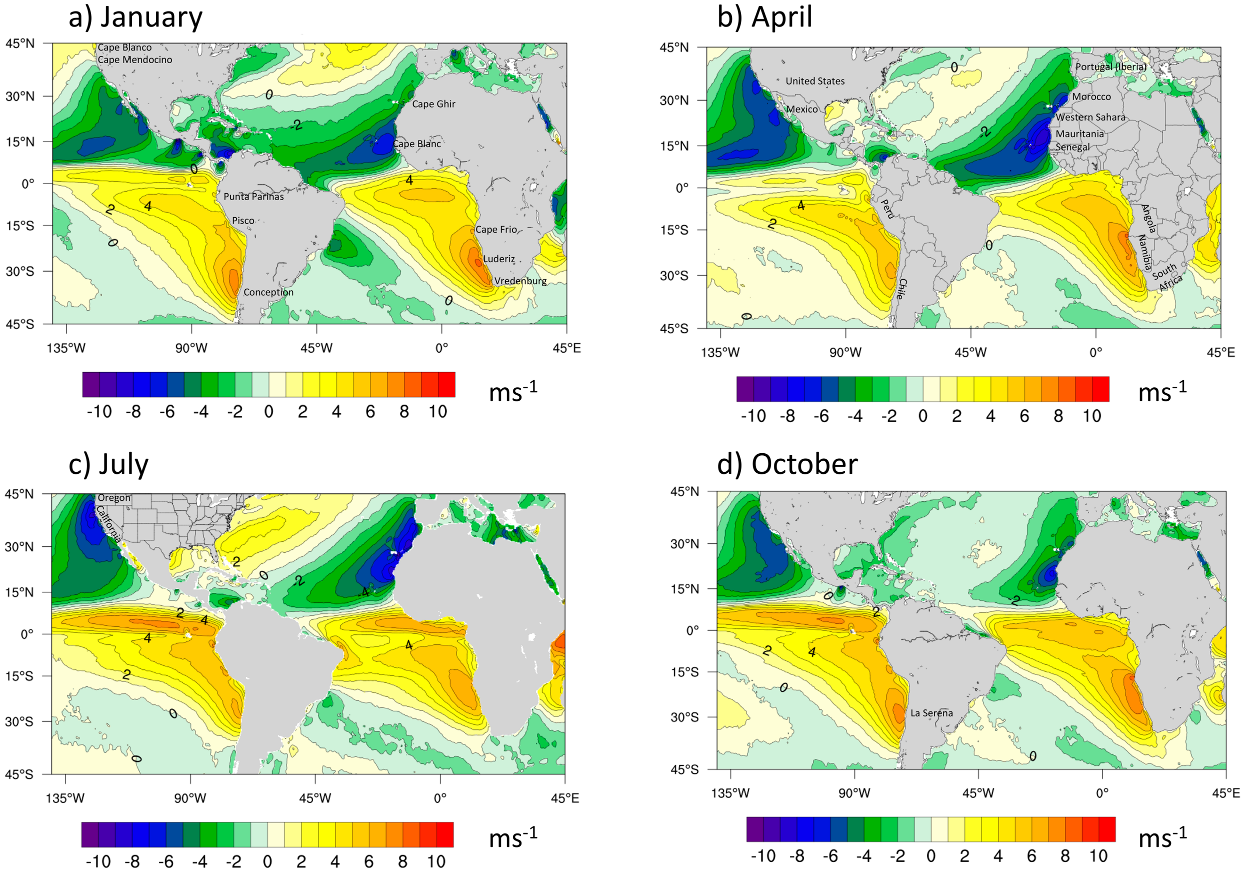
a) January
b) April
c) July
d) October
Cape Blanco
Cape Mendocino
Cape Ghir
Cape Blanc
Punta Parinas
Pisco
Cape Frio
Luderiz
Vredenburg
Conception
United States
Mexico
Portugal (Iberia)
Morocco
Western Sahara
Mauritania
Senegal
Peru
Chile
Angola
Namibia
South Africa
Oregon
California
La Serena
45°N
30°N
15°N
0°
15°S
30°S
45°S
135°W
90°W
45°W
0°
45°E
ms-1
-10 -8 -6 -4 -2 0 2 4 6 8 10

FIG. 1. Monthly long-term mean meridional wind from QuikSCAT SCOW product (Risien and Chelton 2008), for (a) January, (b) April, (c) July, and (d) October. Coastal country/territory names referenced in text are included in (b), U.S. states referred to the text are labeled in (c), and coastal cities and headlands are shown in (a) and (d).

substantial remote impact arising from the Benguela system (Small et al. 2015; Zuidema et al. 2016; Voldoire et al. 2019).

For future climate projections of upwelling, it is important to correctly represent the physical processes occurring at the EBUS. There is considerable debate about how coastal winds will change in the future (Bakun 1990; García-Reyes et al. 2015; Rykaczewski et al. 2015; Bograd et al. 2023). Although fully coupled models are needed to make the projections (e.g., Rykaczewski et al. 2015; Wang et al. 2015; Brady et al. 2017; Chang et al. 2023), with possible options for downscaling (Pozo Buil et al. 2021), forced ocean component simulations are needed for assessing whether the physical processes in present day are represented well (a necessary condition for correct representation of upwelling in the future).

b. Previous studies of EBUS bias in climate models

Climate models, both fully coupled and with forced ocean ice, have exhibited long-standing errors in EBUS. These errors include weak coastal winds, high SST, weak and broad upwelling velocities, weak equatorward surface flow (or in some cases, poleward surface flow, counter to expectation), and insufficient/poorly represented stratocumulus clouds (see Richter 2015; Zuidema et al. 2016; Bonino et al. 2019b).

Some of the important factors and processes for climate model SST bias that have been identified from comparison with observations and/or highly resolved simulations include representation of land topography (e.g., the Andes; Toniazzo 2010), equatorial winds and coastal wave propagation to EBUS (Richter et al. 2012; Toniazzo and Woolnough 2014; Koungue et al. 2019; Illig and Bachèlery 2019; Voldoire et al. 2019; Goubanova et al. 2019), coastal low-level, atmospheric boundary layer jets (Nicholson 2010; Patricola and Chang 2017), local alongshore wind stress (Gent et al. 2010) and wind stress curl (Capet et al. 2004; Small et al. 2015; Kurian et al. 2021; hereafter K21), the oceanic coastal jet (Grodsky et al. 2012; Xu et al. 2014b; Small et al. 2015), mesoscale eddies and feedback to mean flow (Toniazzo et al. 2010), ocean mixing (Deppenmeier et al. 2020), low-level clouds, and radiation and cloud–surface feedbacks (Ma et al. 1996; de Szoeke et al. 2010; Wahl et al. 2011).

c. Coastal upwelling, wind stress curl, and present hypothesis

Classic theory predicts that, in response to switched-on alongshore wind stress forcing, there is flow offshore and upwelling at the coast as a result of Ekman divergence, which is eventually arrested by Kelvin waves generated at the equatorward edge of the wind patch (Allen 1973; Philander and Yoon 1982; Brink 1983). A key feature of the transient upwelling is the existence of a downwind oceanic coastal jet (Charney 1955; Yoshida 1955). Another feature is the coastal undercurrent (Hickey and Pola 1983; McCreary et al. 1987; Gay and Chereskin 2009; Connolly et al. 2014; Chen et al. 2021). The wind stress curl (WSC) has also been found to be important in upwelling zones, as it is related to divergence in the surface Ekman transport and hence to vertical motion (Ekman pumping; Pickett and Paduan 2003; Rykaczewski and Checkley 2008; Jacox et al. 2018; K21). The linear Ekman pumping velocity w_E is given by

$$w_E = \frac{\nabla \times \boldsymbol{\tau}}{\rho_0 f}, \tag{1}$$

where f is the Coriolis parameter, ρ_0 is a reference ocean density, and $\boldsymbol{\tau}$ is the wind stress vector.

Further, the horizontal flow can also be influenced by WSC (Sverdrup 1947; Wunsch 2011; Small et al. 2015; K21). Indeed, the idealized case of a steady state, with no friction or nonlinear terms or bottom torque and on a β plane (approximation that f varies linearly with meridional distance), and with the assumption of no vertical motion at the bottom level of integration, leads to geostrophically balanced meridional flow that is proportional to WSC via Sverdrup balance (Sverdrup 1947):

$$\overline{V} = \beta\rho_0 \int_{-H}^{0} v dz = \nabla \times \boldsymbol{\tau}, \tag{2}$$

where β is the meridional gradient of the Coriolis parameter, v is the meridional current, $\overline{V}$ is vertically integrated meridional flow multiplied by $\beta\rho_0$, and H is the depth of the active ocean layer under consideration. We will refer to vertical and horizontal flow which approximately satisfies (1) and (2) respectively as "WSC-driven."

Analytical solutions of the linearized Boussinesq equations for EBUS have been derived by Fennel and Lass (2007), and Fennel et al. (2012) for upwelling on an f plane in an idealized flat-bottom domain, but including time dependence and friction. They consider an alongshore directed wind with across-shore variation based on the Benguela system. Their solution comprises a coastal upwelling part and a wind stress curl (WSC)-driven part. Specifically, idealized solutions are presented as a function of the distance of the core of the wind jet away from the coast. They found that as the core is displaced farther from the coast, the WSC-driven part plays a more dominant role, leading to a deep poleward flow. For a wind jet close to the coast, there is strong coastal upwelling and an oceanic coastal jet confined within a distance of one Rossby radius from the coast (Allen 1973; Fennel et al. 2012; Bordbar et al. 2021), which is typically a few tens of kilometers (e.g., Allen 1973; Mohrholz et al. 2014).

Recently, the work of Small et al. (2015) and K21 has found that the local coastal bias in some climate and regional models is largely caused by large errors in local WSC, with the atmosphere jet located too far away from the coast. Our hypothesis, deriving from these papers and the theoretical work of Fennel and Lass (2007) and Fennel et al. (2012), is that the high SST bias at the coast in forced ocean models is mainly due to too-weak downwind oceanic coastal jet and too-strong WSC-driven countercurrent, in turn all related to too-weak winds at the coast. Here this hypothesis is tested via examination of a set of global forced ocean-ice simulations that contrast the different wind and WSC fields of two forcing datasets, as well as the response for two different ocean resolutions (coarse versus coastal-eddy-permitting). The focus is on mechanisms such as WSC-driven flow in the horizontal and vertical, and oceanic coastal jets and upwelling, all of which play a role in the model simulations.

d. *Aims and structure of this paper*

The aim of the present paper is to examine the sensitivity of the mean state and variability of simulated upwelling to different forcing datasets and to different ocean model resolutions. In particular, the question is addressed of whether model simulations with a poor mean state can well represent the variability. The focus is on surface variables (primarily ocean temperature and surface stress and its curl, and surface current), which play a large role when coupled in the climate system. (Surface variables have the added advantage of being more regularly observable.) To understand the surface properties, however, it is also necessary to analyze the vertical structure or vertical integrals of properties such as the alongshore flow and vertical velocity, which influence the surface state. We expand on the results of Bonino et al. (2019a,b), who investigated upwelling using a 0.25°NEMO ocean model forced by JRA55-do forcing (~0.5°; Tsujino et al. 2018), and other studies discussed above. The novelty of this current paper is that it is a global assessment of the performance of JRA55-do relative to CORE in EBUS using both eddy-permitting (0.1°) and eddy-parameterized (1°) ocean models. The study further includes a detailed discussion of errors in SST in the Benguela system in the context of supporting regional ocean simulations, as well as overall implications for representation of interannual variability.

The paper is structured as follows: section 2 describes the models, experiments, observations, and methods used. Section 3 gives an overview of the mean state and seasonal cycle of SST in the global Forced Ocean–Sea Ice (denoted FOSI here) runs, including sensitivity of SST to forcing product and to ocean model resolution. Section 4 describes the monthly variability of SST in models and observations, and asks how much the biases in mean state affect simulation of temporal variability of fields of SST in EBUS. It also analyzes vertical velocity variability. Section 5 is a case study of the California Current, a region that has been extensively studied and observed in the past several decades, proposing mechanisms for differences between model solutions and how more realistic simulations are obtained. Section 6 then uses separate Regional Ocean Modeling System (ROMS) simulations to better understand the relatively poor performance of all the global FOSI runs in the Benguela upwelling system. Section 7 is a discussion of whether the effects of WSC are consistent with Sverdrup balance in EBUS in the model solutions. This is followed by conclusions, while a summary of findings for each upwelling system is given in the online supplemental material.

2. Datasets and models

a. Ocean forcing datasets

Results obtained from using two different ocean-forcing datasets are compared here: CORE (Large and Yeager 2004, 2009), and JRA55-do (Tsujino et al. 2018). CORE utilized wind fields at 10 m and air temperature, humidity, and air density at 2 m, from NCEP–NCAR reanalysis, together with surface radiation derived from satellite data and a radiative transfer model (Zhang et al. 2004) and precipitation derived from multiple datasets and observation types (Large and Yeager 2009). It further included adjustments of these fields toward other reference datasets to help remove or reduce known deficiencies of the original dataset (e.g., NCEP–NCAR winds were adjusted toward QuikSCAT wind estimates to increase too-weak wind speeds in the deep tropics and elsewhere, Large and Yeager 2009). In contrast, JRA55-do was based on fields from the JRA55 reanalysis (Kobayashi et al. 2015): some of the advantages of this reanalysis were the higher horizontal resolution (grid spacing around 0.5° compared to 2° for NCEP–NCAR), 3-h output (vs 6 h), and ingestion of a larger number of observations (satellite, in situ). The modified dataset, referred to as JRA55-do (Tsujino et al. 2018), followed a similar adjustment method to CORE but with some differences: the most relevant differences are discussed in section 2c while full details on other aspects are given in Tsujino et al. (2018). We use version 1.3 of JRA55-do. Overall, the new JRA55-do ocean-ice forcing dataset improves upon CORE because it has higher horizontal and temporal resolution and uses state-of-the-art assimilation of a larger number of observations, but it relies on a similar correction method.

b. Model components

1) CESM2

The Community Earth System Model version 2 (Danabasoglu et al. 2020) provides the framework for the global forced experiments below. The coupling infrastructure is the Common Infrastructure for Modeling the Earth (CIME, version 5), a new collaborative software for building and running the system as well as controlling state and flux exchanges between components (Danabasoglu et al. 2020). Air–sea fluxes are computed in CIME with the Large and Yeager (2004, 2009) scheme. A discussion of how this compares with other schemes can be found in Fu et al. (2021).

2) POP-CICE

The global ocean model is based on Parallel Ocean Program version 2 (Smith et al. 2010; Danabasoglu et al. 2012). The standard resolution POP2 is on a nominal 1° grid (actually 1.11° in the zonal direction and with a meridional grid spacing varying between 0.27° at the equator and 0.54° at higher latitudes). It has 60 vertical levels, with 10-m grid spacing in upper 100 m. The main parameterizations are of vertical mixing [*K*-profile parameterization (KPP); Large et al. 1994], mesoscale eddies (Gent and McWilliams 1990), submesoscale eddies (Fox-Kemper et al. 2008), and dense overflows (Danabasoglu et al. 2010). High-resolution POP has nominal 0.1° horizontal resolution (decreasing from about 11 km at the equator to 2.5 km at high latitudes) and uses a tripolar grid with two poles in the Northern Hemisphere over North America and Asia to overcome the North Pole singularity, and 62 vertical levels, ranging from 10-m spacing in the upper 200 m to 250-m spacing in the deep ocean, with the use of partial bottom cells. In many regions of the world this model may be considered eddy-resolving, but for coastal EBUS where the Rossby radius is small (typically between 20 and 50 km) it is more strictly eddy-permitting. Bathymetry was interpolated from the ETOPO2v2 dataset with BEDMAP (Lythe et al. 2000) used at polar regions. The high-resolution model uses the same KPP physics as the standard resolution, but does not include any mesoscale, overflow, or submesoscale parameterizations. POP computes heat and momentum surface fluxes based on state variables from the forcing dataset (e.g., CORE, JRA55-do), SST and surface current from POP and the Large and Yeager (2004, 2009) bulk formulas. More details on the ocean model configurations are contained in Chassignet et al. (2020). The sea ice model is CICE5 (Hunke et al. 2015), run on the same grid as the companion ocean model.

3) ROMS

ROMS is used in this paper to focus on the Benguela system processes in a more constrained manner than the global simulations. ROMS (Shchepetkin and McWilliams 2005; Haidvogel et al. 2008) is a primitive equation, hydrostatic, free-surface, split-explicit ocean model with horizontal curvilinear coordinates and terrain-following "z-sigma" vertical coordinates (Lemarié et al. 2012; Shchepetkin and McWilliams 2009). The ROMS component uses identical settings in all configurations: harmonic horizontal mixing of momentum and tracers, the KPP scheme (Large et al. 1994) for vertical mixing, the fourth-order Akima horizontal and vertical tracer advection (Shchepetkin and McWilliams 2005), and 50 layers in the vertical. ROMS computes surface fluxes based on state variables from the forcing dataset, SST from ROMS and the Fairall et al. (2003) surface flux routine. (The changes caused by using a different surface flux algorithm to CESM/POP are discussed in section 6.) Open boundary conditions are provided using a hybrid of radiation and nudging approaches (Marchesiello et al. 2001) for the three-dimensional velocity and tracers, the Chapman (1985) scheme for the free surface, and the Flather (1976) scheme for the two-dimensional velocities.

4) POP-CICE AND ROMS EXPERIMENTS

This paper employs FOSI experiments performed as part of the International Laboratory for High-resolution Earth System Prediction (iHESP) project (Chang et al. 2020) and

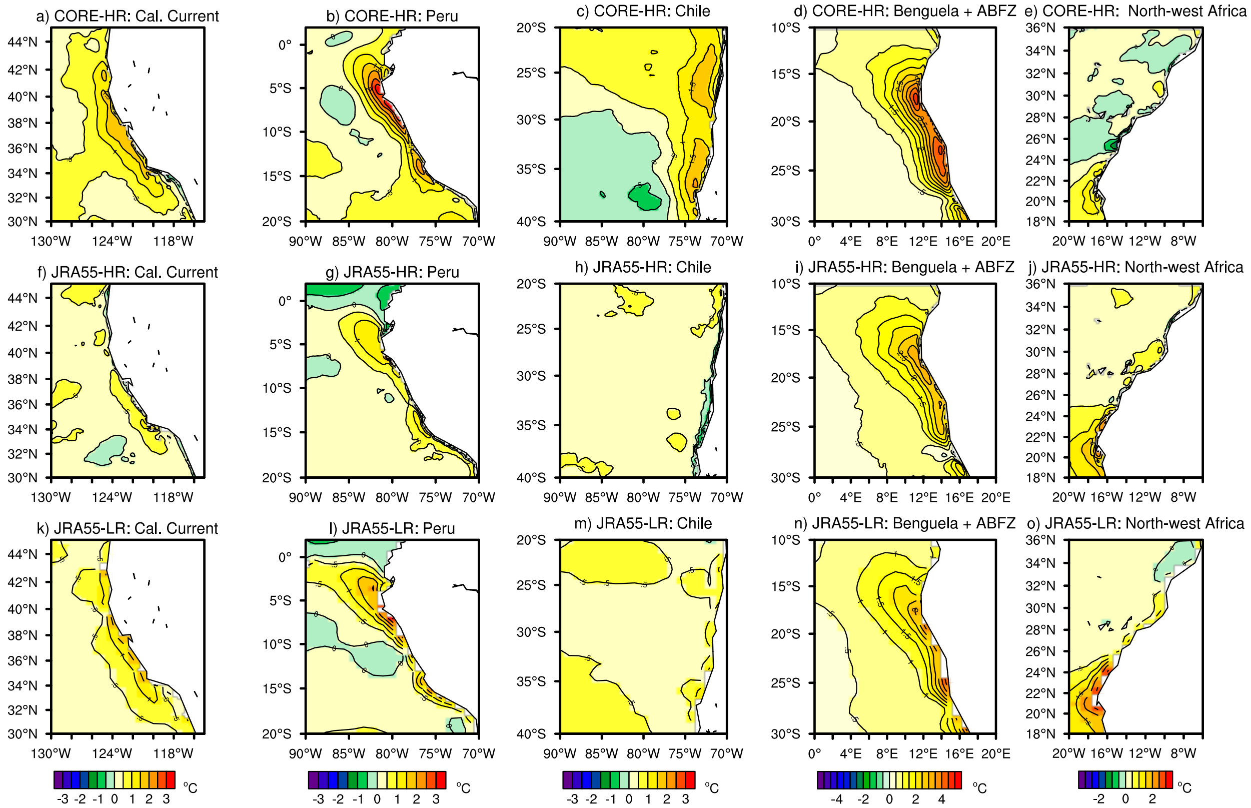
a) CORE-HR: Cal. Current
b) CORE-HR: Peru
c) CORE-HR: Chile
d) CORE-HR: Benguela + ABFZ
e) CORE-HR: North-west Africa
f) JRA55-HR: Cal. Current
g) JRA55-HR: Peru
h) JRA55-HR: Chile
i) JRA55-HR: Benguela + ABFZ
j) JRA55-HR: North-west Africa
k) JRA55-LR: Cal. Current
l) JRA55-LR: Peru
m) JRA55-LR: Chile
n) JRA55-LR: Benguela + ABFZ
o) JRA55-LR: North-west Africa
44°N 42°N 40°N 38°N 36°N 34°N 32°N 30°N
130°W 124°W 118°W
0° 5°S 10°S 15°S 20°S
90°W 85°W 80°W 75°W 70°W
20°S 25°S 30°S 35°S 40°S
10°S 15°S 20°S 25°S 30°S
0° 4°E 8°E 12°E 16°E 20°E
36°N 34°N 32°N 30°N 28°N 26°N 24°N 22°N 20°N 18°N
20°W 16°W 12°W 8°W
-3 -2 -1 0 1 2 3 °C
-4 -2 0 2 4 °C
-2 0 2 °C

FIG. 2. Sensitivity of SST bias to the forcing dataset (shown in the top two rows) and ocean model resolution (shown in the bottom two rows). Model results are from 2000 to 2009, and the bias is relative to the Banzon et al. (2014) OISST climatology. Results are from (a)–(e) the CORE-forced high-resolution ocean (CORE-HR), (f)–(j) the JRA55-do-forced high-resolution ocean (JRA55-HR), and (k)–(o) JRA55-do-forced low-resolution ocean (JRA55-LR) for the California Current, Peru, Chile, Benguela and ABFZ, and northwest Africa (shown from left to right, respectively). All panels are annual means and share the same color bar for ±3°C shown at the bottom, except for Benguela cases expanded to ±5°C.

c. *SST sensitivity to surface heat fluxes*

The changes of SST between model cases noted above can be due to ocean dynamical processes (section 5), or thermodynamic processes related to the forcing, or their combination. A full heat budget has not been done here (see K21 instead for an illustrative heat budget for the Benguela), but some inference on the budget can be made simply by examining the changes to net surface heat flux (SHF), a major term in the budget. If the change in SHF between JRA55-do and CORE-forced simulations [ΔSHF = SHF(JRA55-do) − SHF(CORE)] is such as to cool the surface (negative in our sign convention), it might help explain lower SST in the JRA55-do case. On the other hand, if ΔSHF is positive (warming the ocean) but the SST is lower in the JRA55-do case, then the SHF is acting as a damping. In this latter case ocean dynamical processes must give rise to the lower SST in the JRA55-do-forced simulations.

For the high-resolution ocean cases the surface heat flux is damping the SST difference between JRA55-do and CORE, causing a general warming tendency of the narrow coastal zone in the JRA55-do-forced case, relative to CORE (Figs. 3a–e), where the SST is lower (Figs. 3f–j). These results are indicative of the feedback of surface fluxes to SST, due to the modulation of the turbulent heat fluxes (latent and sensible) and upwelling longwave, with typical values of about 30 W m^{-2} $°C^{-1}$ (Large and Yeager 2012). For the low-resolution cases JRA55-LR and CORE-LR, the surface heat flux differences were typically smaller (see supplemental text part S3 and Fig. S5), with a minimal influence of the feedback: and for Benguela and Peru there was some evidence of ΔSHF acting to aid the SST difference by causing a cooling near the coast.

d. *Seasonal cycle of SST*

Seasonal cycle curves (Fig. 4) reveal that model errors occur throughout the year, but they are largest in the summer season for the California Current (Fig. 4a, Table 3b) and Chile (Fig. 4c, Table 3b) and in the winter season for the Peru (Fig. 4b, Table 3c) and ABFZ (Fig. 4e, Table 3c) regions. JRA55-HR has impressive simulation of SST in both the California Current (Fig. 4a, excepting an ~1°C warm bias present year-round) and off Chile (Fig. 4c, with only a small mismatch with observations in JFM). This includes a good representation of the phase of the seasonal cycle off California,

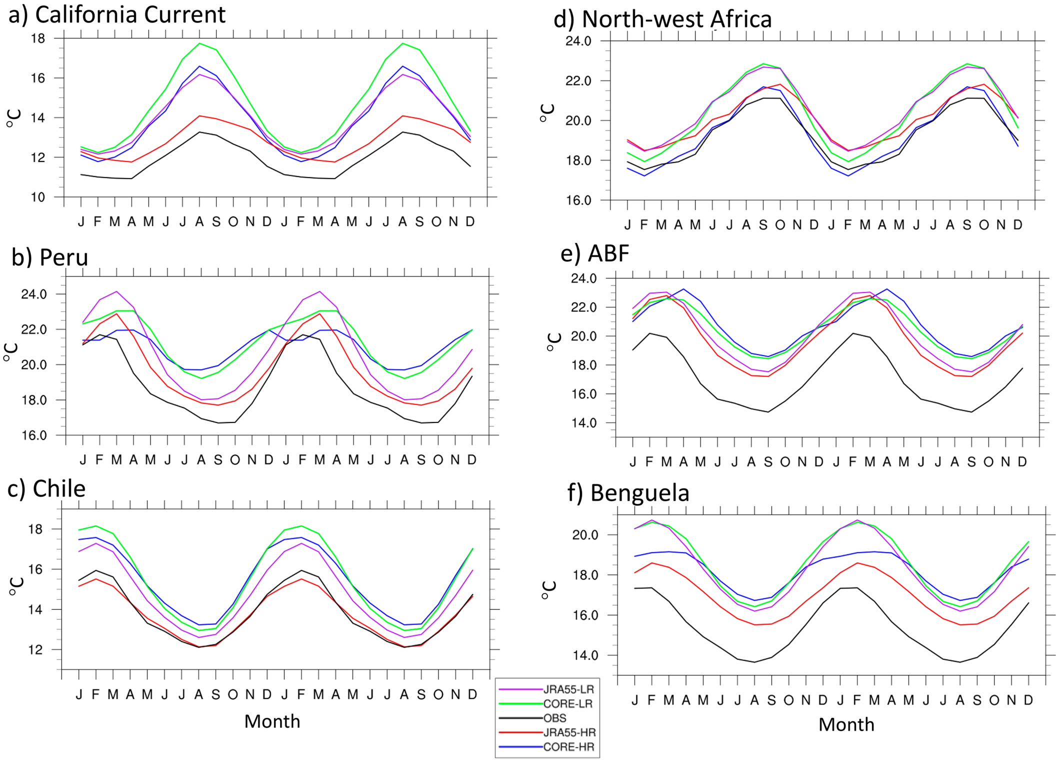

FIG. 4. The average seasonal cycle of SST averaged over the upwelling zones as labeled from monthly averaged data for years 2000–09. Two annual cycles are shown for clarity, with months marked by their initials. The legend refers to the model case (Table 1) or observations (OBS).

Chile (Fig. 4c), JRA55-LR, CORE-HR, and CORE-LR exhibit errors rising from ~1°C in austral winter to ~2°C in austral summer (Table 3b,c).

Off northwest Africa the low-resolution models perform worse, as noted in section 3b, while CORE-HR performs better than JRA55-HR in capturing the seasonal cycle (Fig. 4d, Table 3). Off Peru and in the ABFZ and Benguela the model errors are more complex (Figs. 4b,e,f). Notably the seasonal cycle in the CORE-forced simulations have poor phasing and weak amplitude off Peru while the JRA55-do forced cases are too warm especially around February–April (Fig. 4b). In the ABFZ all models overpredict SST throughout the year (and the CORE cases have a lag in the seasonal maximum; Fig. 4e), while in the Benguela JRA55-HR has a notably lower bias than other cases in all months (Fig. 4f).

The above analysis can be linked more precisely to upwelling and coastal processes alone, by studying the cross-shore difference (or gradient) of SST between an offshore point well away from the main coastal upwelling, and the coast. For the former we use SST 200 km to the west of the coast. The seasonal cycle analysis of SST gradient reveals that the low-resolution models always underpredicted the gradient (Fig. 5). JRA55-HR reproduces the offshore SST-gradient best, relative to observations, in the California Current, Peru, and ABFZ regions (Figs. 5a,b,e), but exhibited an overprediction of gradient off Chile throughout the year (Fig. 5c). Both CORE-HR and JRA-HR overestimated the seasonal cycle of gradient off northwest Africa (Fig. 5d) and, very notably, in the Benguela region (Fig. 5f), which has a very weak seasonal cycle in observations. Of possible relevance to the latter is that the adjustment of winds in JRA55-do leads to a good representation of strong wind stress off Luderitz (~26°S) in DJF, but is too weak in JJA compared to satellite data (see supplemental material labeled "All Regions"): this may lead to the overly large seasonal cycle of SST gradient in the Benguela in JRA55-HR. In the ABFZ, only JRA55-HR was able to capture the weak seasonal cycle of SST gradient in observations (Fig. 5e). Part of the reason for weaker gradients in observations than in JRA55-HR off Chile (and to a lesser and seasonally confined extent off California and Benguela) may be due to inherent smoothing in OISST as well as problems with assessing SST under cloud cover (see section 2 herein; Reynolds et al. 2007, 2013).

4. Time series of SST and vertical velocity variability

In this section the monthly to interannual variability of SST at the EBUS is described, for model and observations, as well as some indices of upwelling, such as vertical velocity estimates.

a. *Monthly SST variability*

The findings above reveal that the mean state of SST in most EBUS is, in general, better represented when using

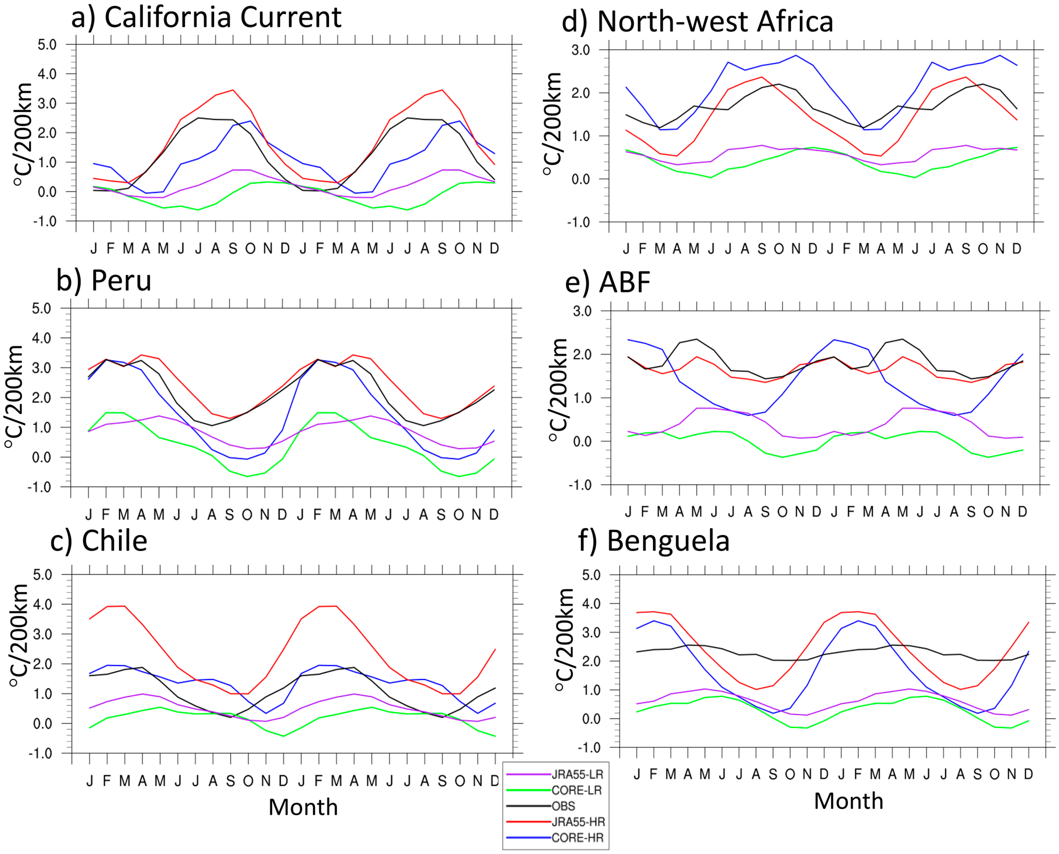

FIG. 5. The average seasonal cycle of SST gradient across-shore, averaged over the upwelling zones as labeled, from monthly averaged data for years 2000–09. Two annual cycles are shown for clarity, with months marked by their initials. The gradient here is defined as the SST 200 km west of the coast minus SST at the nearest grid point to the coast.

JRA55-do forcing, and the additional use of a high-resolution ocean leads to further improvement in most regions. A follow-on question is whether the variability of SST is also improved. This is addressed here by analyzing time series of SST anomalies from the upwelling regions. Monthly and longer time scales are considered, as being of potential interest for the topic of seasonal-to-decadal climate prediction in EBUSs. The period 1993–2018 is analyzed (to cover the overlapping period of satellite SST, SSH, and JRA55-do model simulation), but note the CORE-forced runs finish in 2009. Similar conclusions were obtained when all datasets were restricted to the common 1993–2009 period.

The anomaly time series of SST shows strong interannual variability in all cases (Fig. 6), and there is a high degree of similarity between different simulations. The models exhibit correlations of SST with observations of 0.5 or above everywhere (Table 4a), perhaps higher than might be expected if processes related to mean bias also governed the variability. For example, CORE-LR shows large mean SST bias in the California region (Table 3, Fig. S3), but a 0.71 correlation with observations for variability (Table 4a), and all simulations have a large bias in the Benguela and ABFZ (Fig. 2, Table 3, Fig. S3), but correlations in that region are 0.5 or above.

The northwest Africa region has highest correlations overall (between 0.88 and 0.92), followed by California (0.71–0.93), and Benguela the lowest (0.5–0.7: ABFZ has some slightly higher values), see Table 4a. In all regions JRA55-do forced simulations perform better than CORE-forced, although this is only marginal off northwest Africa (Table 4a). An interesting aspect is that the high-resolution ocean does not always perform better than low resolution for the same forcing dataset. Specifically, with the JRA55-do forcing, HR only marginally improves the simulated variability over LR in two regions, and is slightly worse for the Benguela, ABFZ, and northwest Africa, but differences are generally small. With CORE forcing the results are even more nuanced with HR actually degrading the simulated variability at all locations except the California Current System.

The likely explanation for the similarity of the time series from different model cases is that the SST variability is part of large-scale climate mode patterns, which appear to be well represented in all cases. Taking the California Current as an example, these include the Pacific warm "Blob" (2014–16, marked on Fig. 6a; see Bond et al. 2015; Hartmann 2015) which impacted the U.S. West Coast (Di Lorenzo and Mantua 2016; Gentemann et al. 2017), or remote forcing from other

Enfield and Allen 1980; Chelton and Davis 1982; Ramp et al. 1997; Strub and James 2002; Frischknecht et al. 2015; Amaya et al. 2022). There are also oceanic responses to nonlocal atmospheric teleconnections which can lead to changes in ocean circulation which then affect the EBUS [all these processes are discussed in, e.g., Frischknecht et al. (2015)]. CTWs also influence the other EBUS such as off Peru and Chile (Shaffer et al. 1997; Colas et al. 2008) and the ABFZ and Benguela (Rouault 2012; Illig and Bachèlery 2019).

The remote influences include those of the strong 1997/98 and 2015/16 El-Niño on the Peru, Chile, and California time series (Figs. 6a–c). The Niño-3.4 and Niño-1 + 2 indices are shown in Fig. S6 for reference, together with their correlations with the EBUS SST time series. SST in the California upwelling zone is correlated at values between 0.48 and 0.61 with Niño-3.4 SST (for lag 0, using monthly data): for Peru correlations range from 0.7 to 0.9 against Niño-1 + 2 (the Niño-1 + 2 region overlaps the Peru upwelling): for Chile, from 0.52 to 0. 71, again with Niño-1 + 2. There is no notable lag between peaks in the Niño-3.4 index and peaks in California SST for the 1997/98 and 2015/16 events, suggesting an atmospheric teleconnection rather than the lagged oceanic teleconnection of Chelton and Davis (1982) seen in earlier El-Niño events, but at other times of the record there does appear to be a lag between Niño-3.4 and California SST, e.g., the 1999–2000 La Niña (see Fig. S6c). This suggests that different types of teleconnections are dominant for different events (D. Chelton 2022, personal communication). The type of teleconnection can also differ depending on which part of the California Current is considered, from Southern California to Washington State (Jacox et al. 2019), and our single area-average may mix different processes occurring in different subregions. We do not attempt to distinguish the different types of teleconnections, as the time scales of the teleconnections may be too fast to be identified in the monthly mean data analyzed here. Other regions are affected by large scale variability: the North Atlantic Oscillation, Atlantic meridional mode, and Atlantic multidecadal variability affect the northwest Africa upwelling (Bonino et al. 2019a), while the ABFZ and Benguela exhibit “Benguela Niño” behavior (Shannon et al. 1987; Florenchie et al. 2003; Richter et al. 2010; Koungue et al. 2019).

It may be argued that SST variability is an easy target for forced ocean models, because of the tight constraint to the forcing variables (such as near-surface air temperature), as mentioned in section 1. To address this, we also looked at variability of sea surface height (SSH), since in these regions SSH is related to thermocline depth and currents and is less constrained by the forcing. The time series are shown in Fig. S7, and correlations with observations are included in Table 4b, and they reinforce the SST results, with, for example, correlations of SSH with observations off California, Peru, and Chile all higher than 0.76 (Table 4b). We also compared temperature at 50-m depth with that from a high-resolution reanalysis (Lellouche et al. 2021) and similarly found that the FOSI simulation well represented the 50-m temperature variability in all except the Benguela region (Fig. S8, Table S1).

Another key point is that in most regions SST and SSH covary quite closely (e.g., correlations between observed SST and SSH are above 0.8 for the California and Peru systems, 0.7 for Chile, although only 0.41 for the Benguela). In addition, model temperature variability at various depths down to 100 m (below the typical mixed layer) is correlated with model SST (correlations above 0.7 in California, Peru, and Chile systems) indicating that the thermocline depth is also varying such that warm SST is connected to deeper thermoclines and higher SSH. This further supports the likelihood that SST has a strong influence from thermocline depth variability, since in a first mode baroclinic process the thermocline depth is correlated with SSH (e.g., for CTWs; Amaya et al. 2022).

b. *Monthly vertical velocity variability*

The model results can also be compared with estimates of vertical transport (upwelling) made by Jacox et al. (2018) for the California Current system. The coastal upwelling transport index is a refinement of the long-standing Bakun upwelling index (Bakun 1973) to include the combined effect of coastal Ekman transport, Ekman pumping, and response to zonal geostrophic flow. The CUTI is derived from a data-assimilating ROMS simulation which is forced either by global atmosphere reanalysis or by a regional data-assimilating atmosphere model. Rather than using the ROMS vertical velocities, the CUTI estimates the transport from surface stress and also uses model geostrophic flow and mixed layer depth as input (Jacox et al. 2018). However, for the FOSI models being discussed here we do use model vertical velocity directly, at 30 m, as a proxy for vertical velocity at the base of the mixed layer (Ding et al. 2021). The vertical velocity is averaged over 100 km west of the coast [note that Jacox et al. (2018) use 75 km but we use 100 km to better match the approximate grid size of the low-resolution ocean grid; additionally we use as many high-resolution ocean model grid cells as fit in 100 km]. The CUTI is essentially vertical transport ($\mathrm{m^3\,s^{-1}}$) per meter of coastline, for a 75-km box offshore. For comparison with the model area-averaged vertical velocities (given in $\mathrm{m\,day^{-1}}$), the CUTI values ($\mathrm{m^2\,s^{-1}}$) are divided by the offshore grid box width 75 000 m and then multiplied by 86 400 (seconds in a day) to give equivalent area-averaged vertical velocities ($\mathrm{m\,day^{-1}}$).

Inspection of the vertical transport time series (Figs. 7a,b) reveals that all the global FOSI models reproduce the phasing of both the seasonal cycle and the month-to-month variability. The seasonal cycle amplitude is underestimated in all simulations, but JRA55-HR comes closest to the CUTI (Fig. 7a). The amplitude of the monthly-to-interannual variability is also captured quite well although some particular events in the CUTI record are much weaker or even absent in the global model time series (e.g., between years 2000 and 2003 and in mid-2006; Fig. 7b). The correlation of model vertical transport with CUTI is 0.75 for both JRA55-LR and JRA55-HR and 0.6–0.65 for the CORE-forced simulations.

The model vertical velocity variability has similar phasing to that of meridional wind stress (cf. Figs. 7b,c), as expected (Bakun 1973; Jacox et al. 2018). Thus we suggest that the overall good performance of global FOSI in representing the

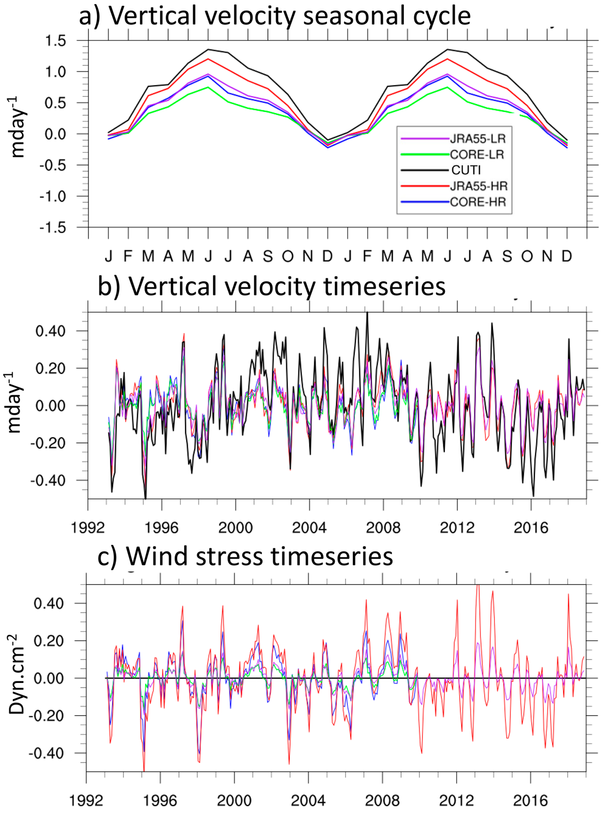

FIG. 7. Upwelling transport expressed as upwelling velocity area averaged over the defined California Current coastal region. (a) Seasonal cycle of upwelling from CUTI and model simulations (w at 30 m). (b) Time series of monthly vertical velocity anomalies from climatology. (c) Meridional wind stress (negated so positive is southward and upwelling favorable) anomaly time series.

vertical transport of CUTI (Fig. 7b) is due to the strong dependence on surface wind stress, which is derived from reanalysis in both the global model experiments and the CUTI product. Conversely, the differences between global model vertical transport and CUTI during particular events in Fig. 7b may be due either to quantitative differences in wind stress forcing or to differences in the geostrophic transport contribution, which is not expected to be similar (as the global model simulations do not employ data assimilation, unlike the ROMS simulation used in CUTI). Further research is required to distinguish these different effects.

5. California Current case study and comparison with other regions

In this section, reasons for the differences in model mean state identified in section 3 are examined for a case study of the California Current, focusing on the summer upwelling season. In this section, 10-yr means (2000–09) are considered.

a. California Current case study

For the California Current, JRA55-HR captures the observed low SST near the coast of 12°–14°C in the peak of the upwelling season, June–August (JJA; see Figs. 8c,e). The important feature, beyond just absolute SST, is the fact that isotherms are packed parallel to the coast in this simulation, as in observations. Neither CORE-HR (Fig. 8d) or the use of the standard 1° ocean model (CORE-LR and JRA55-LR; Figs. 8a,b) can replicate these results, and both exhibit too high SST and weak SST gradients. Reasons for these differences are explored later in this subsection. When differenced against observed SST, JRA55-HR errors are mostly less than 1°C excepting small patches around 34°N and north of 42°N (Fig. 8f).

Focusing next on the meridional wind stress in this season (Fig. 9), JRA55-LR shows a southward core with a maximum around 39.5°N (Fig. 9b), south of Cape Mendocino. However, it does not well capture the secondary maximum at 42°N (south of Cape Blanco) that is visible in QuikSCAT (Fig. 9c). The JRA55-do-forced cases have stronger southward stress along the coast (and a much reduced drop-off of wind toward the coast), compared to those forced by CORE (Figs. 9a,b,d,e). This is more favorable for coastal upwelling over WSC-driven upwelling, helping to maintain low SST.

It can be seen from Fig. 9 that the strengthening of equatorward wind stress at the coast in JRA55-do relative to CORE is more notable for the 0.1° ocean simulation (Figs. 9e,f). Recalling that JRA55-do grid spacing is ~0.5°, and that the low-resolution ocean has ~1° grid spacing, it is clear that the detailed spatial structure of wind in JRA55-do will be degraded on the low-resolution ocean grid but will be maintained on the 0.1° high-resolution grid. This may explain the sensitivity of wind stress strengthening to ocean grid size. An example of this is a hint of the secondary wind maximum at 42°N in the 0.1° model forced by JRA55 (JRA55-HR; Figs. 9e,f) which is barely visible on the 1° grid (Figs. 9a,b).

The southward wind stress drives the California Current, which in JRA55-LR is a single, broad southward flow of around 10 cm s^{-1} (Fig. 10a). With JRA55-do forcing the current is strengthened by a few centimeters per second over the CORE case (Fig. 10b). In JRA55-HR, two distinct features are seen, a narrow southward coastal current extending from Vancouver Island to Oregon, and an offshore branch (Fig. 10c), as discussed, for example, in Marchesiello et al. (2003). The stronger currents in high resolution, about 20 cm^{-1} off Oregon coast and ~15 cm^{-1} in the California Current, are more consistent with observations. Long-term measurements of surface southward currents in summer of between 20 and 40 cm^{-1} have been described at line "P" (latitude of Newport, Oregon, 44.65°N; Huyer et al. 2007) and of about 10 cm^{-1} south of 34°N in CalCOFI by Gay and Chereskin (2009). In JRA55-HR the coastal southward flow is strengthened by over 10 cm^{-1} relative to CORE-HR (Fig. 10d).

What drives the enhanced coastal flow with JRA55-do? Two processes are important and occur concurrently: stronger near-coastal alongshore wind stress, and changes to WSC. The former leads to the oceanic coastal jet within a baroclinic Rossby radius (a few tens of kilometers; section 1c) of the coast, while the latter affects the depth-averaged flow. The meridional wind stress in CORE at the coast is at least one-third weaker than in JRA55-do (Figs. 9d–f), which will lead to

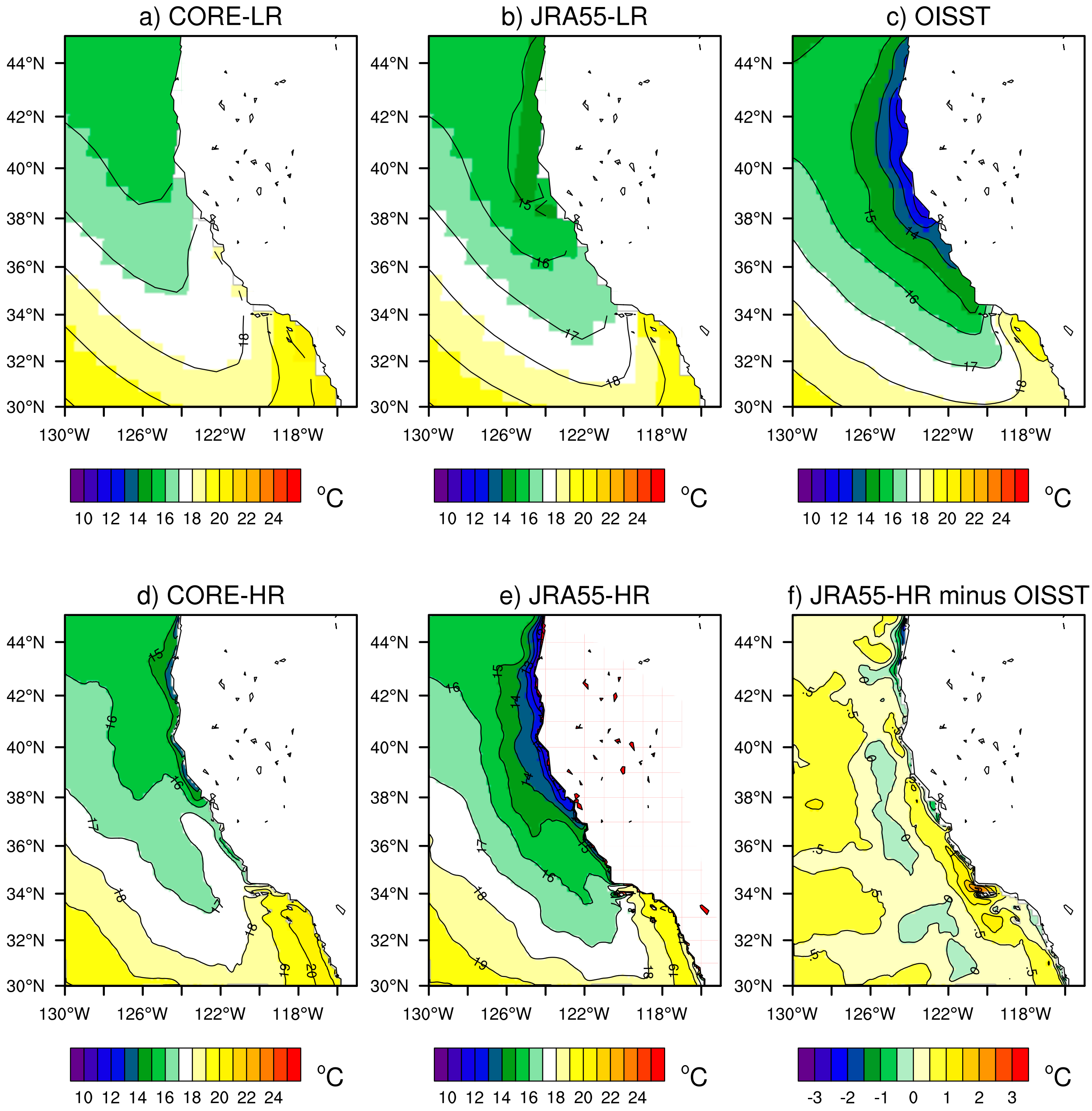

FIG. 8. California Current SST. Seasonal JJA average of SST from a 10-yr (2000–09) segment for the (a),(b) 1° ocean model and (d),(e) 0.1° model, using CORE in (a) and (d) and JRA55-do in (b) and (e). (c) Corresponding field from OISST (Banzon et al. 2014; Reynolds et al. 2007). (f) Difference of JRA55-HR and observed OISST for JJA. Here the color shading shows individual model grid cells while the line contours have been spatially smoothed.

a weaker oceanic coastal jet. There are related changes in the WSC (Figs. 11a–c, based on JRA55-HR and CORE-HR: note that the low-resolution models are not shown here). Using JRA55-do leads to a smaller cross-shore scale of the wind drop-off, shown as a strengthened but narrower band of positive WSC within about 0.5°–1° of the coast (Fig. 11b), resulting in a dipole of differences with CORE-HR (positive right at coast, negative in a thicker band offshore; Fig. 11c). The observations from QuikSCAT confirm that the band of positive wind stress curl (mostly equivalent to the zonal gradient of meridional wind stress) occurs over a narrow band close to shore (Fig. 11d), especially adjacent to the wind stress maxima (Fig. 9c). [Note that the landmask for this QuikSCAT product (Risien and Chelton 2008) covers the area of some of the nearest coastal cells of the 0.1° ocean model.]

As described in section 1c, the WSC can affect both the horizontal flow and vertical motion. First, the applicability of Sverdrup balance to the meridional flow is examined, using

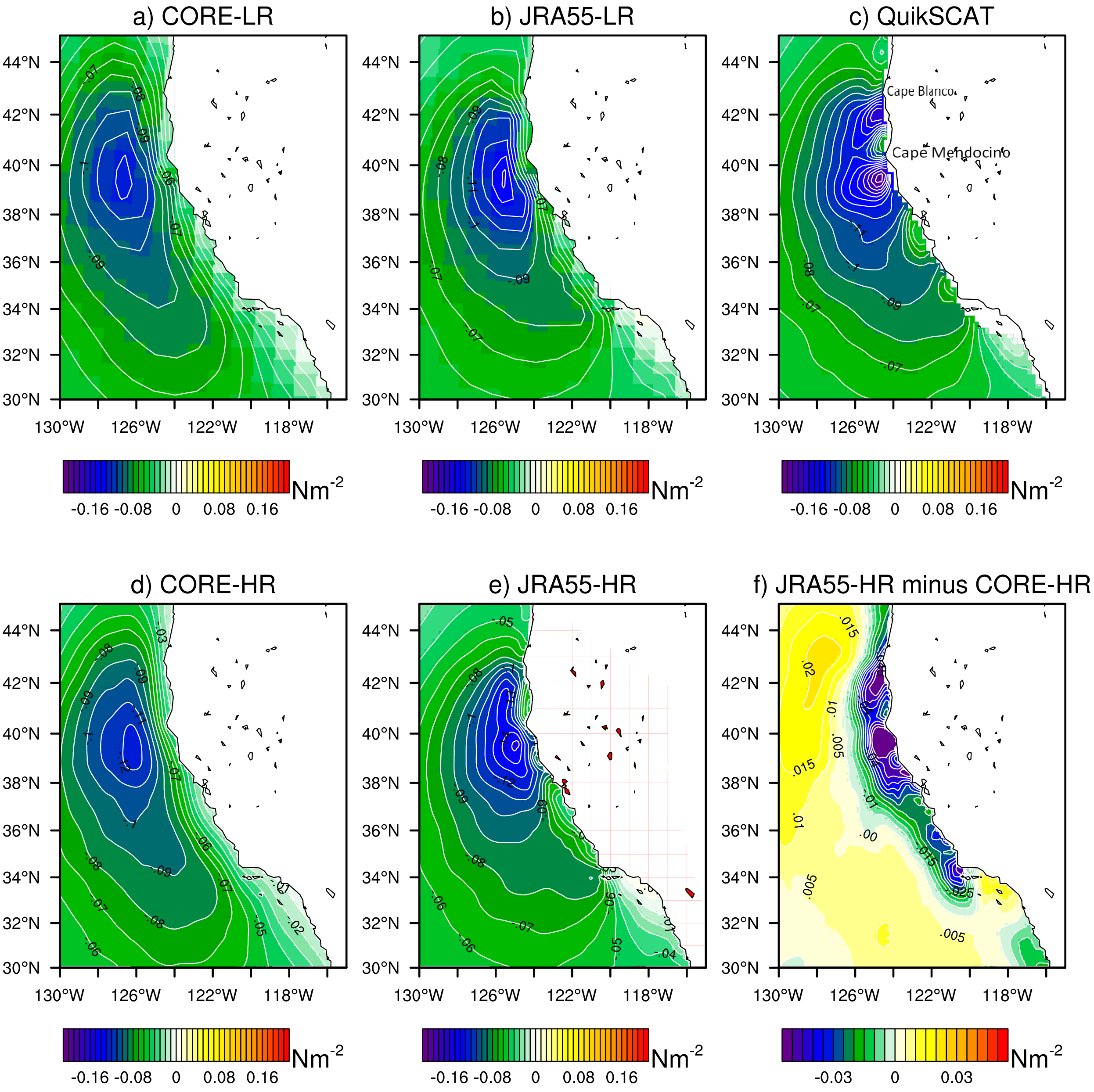
a) CORE-LR
b) JRA55-LR
c) QuikSCAT
d) CORE-HR
e) JRA55-HR
f) JRA55-HR minus CORE-HR
Cape Blanco
Cape Mendocino
44°N
42°N
40°N
38°N
36°N
34°N
32°N
30°N
130°W
126°W
122°W
118°W
Nm-2
-0.16 -0.08 0 0.08 0.16
-0.03 0 0.03

FIG. 9. California Current wind stress. Seasonal JJA average of meridional wind stress from a 10-yr (2000–09) segment for (a),(b) a 1° ocean model and (d),(e) a 0.1° model, using CORE in (a) and (d) and JRA55-do in (b) and (e) and showing (f) JRA55-do minus CORE. (c) Corresponding field from QuikSCAT (Risien and Chelton 2008). Here the color shading shows individual model grid cells while the line contours have been spatially smoothed.

(2) with H set to 400 m (see Fig. S9 for other depths). Sverdrup balance is not expected to hold close to the coast, such as within a Rossby radius, due to the influence of other factors such as the oceanic coastal jet and the undercurrent (Fennel and Lass 2007). However it may hold further away from the coast, a possibility which is investigated here, for long-term 10-yr means [a related approach was applied by Penven et al. (2005) and Veitch et al. (2010)].

Figures 11e and 11f show the integrated meridional velocity $\overline{V}$ that is to be compared with the WSC (Figs. 11a–c). This reveals a band of positive $\overline{V}$ extending 2°–3° of longitude away from the coast in CORE-HR and JRA55-HR (Figs. 11e,f). The width of this band is comparable to the width of positive WSC in the simulations (Figs. 11a,b). For both $\overline{V}$ and WSC the band is narrower in JRA55-HR than in CORE-HR. As a consequence, the difference in WSC between simulations (Fig. 11c) has some similarity to the difference in $\overline{V}$, both showing a negative band extending about 3° of longitude away from the coast. This all suggests a qualitative agreement with Sverdrup balance beyond the first Rossby radius (20–30

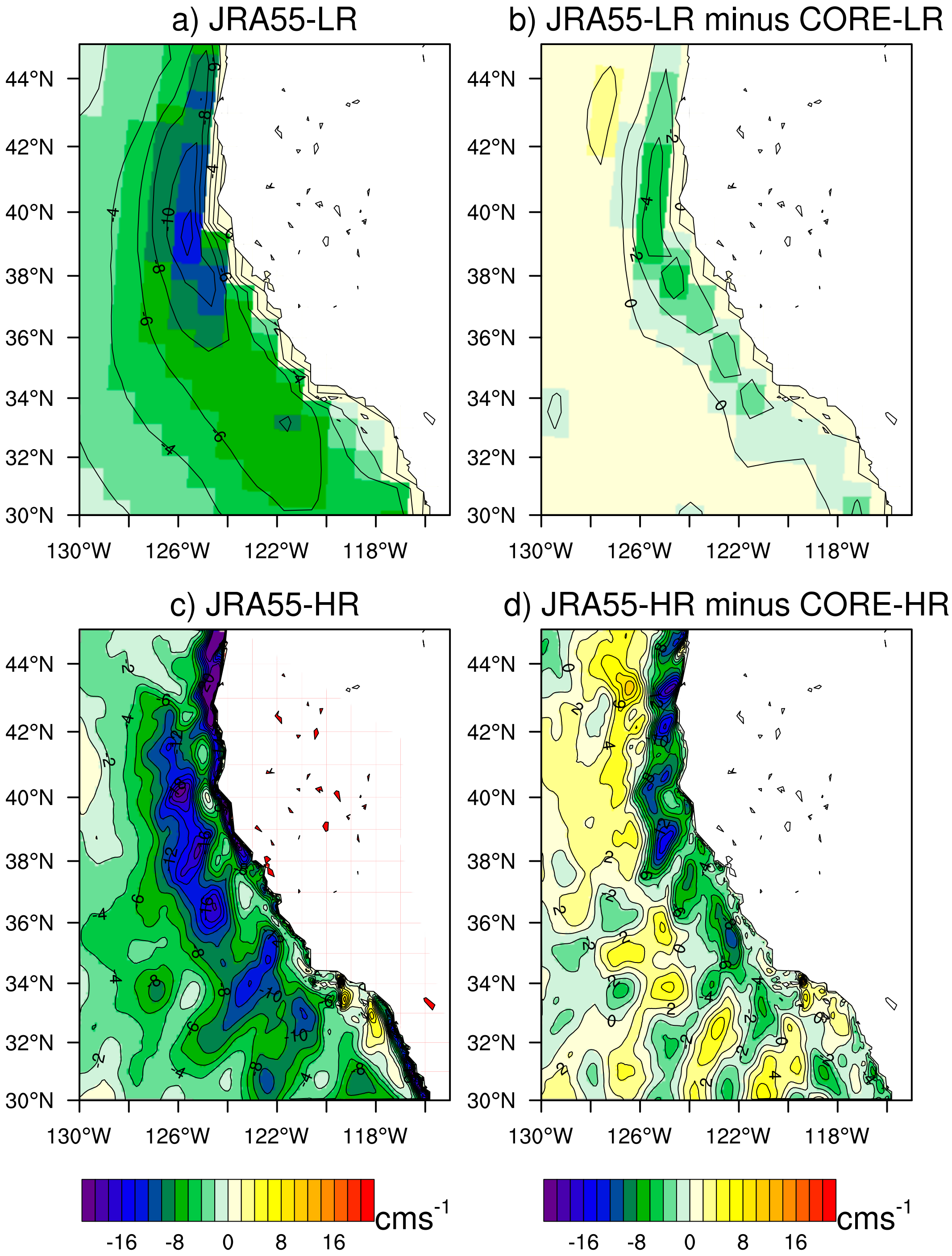
a) JRA55-LR
b) JRA55-LR minus CORE-LR
c) JRA55-HR
d) JRA55-HR minus CORE-HR
44°N
42°N
40°N
38°N
36°N
34°N
32°N
30°N
130°W
126°W
122°W
118°W
cms^{-1}
-16
-8
0
8
16

FIG. 10. California Current surface meridional velocity. Seasonal JJA average from the 10-yr (2000–09) segment for a (a),(b) 1° ocean model and (c),(d) 0.1° model, for (left) JRA55-do and (right) JRA55-do minus CORE. All panels share the same color bar.

km) but within 3° of the coast. Despite this there are several important quantitative differences between the WSC and $\overline{V}$: e.g., the WSC is stronger at the coast in JRA55-HR between 38° and 42°N, but $\overline{V}$ is weaker, and further than about 3° from the coast there is very weak negative WSC but a relatively strong $\overline{V}$ (also negative) in both simulations (Figs. 11a,b,e,f). These results indicate that the California Current has much more complex dynamics than described by Sverdrup balance

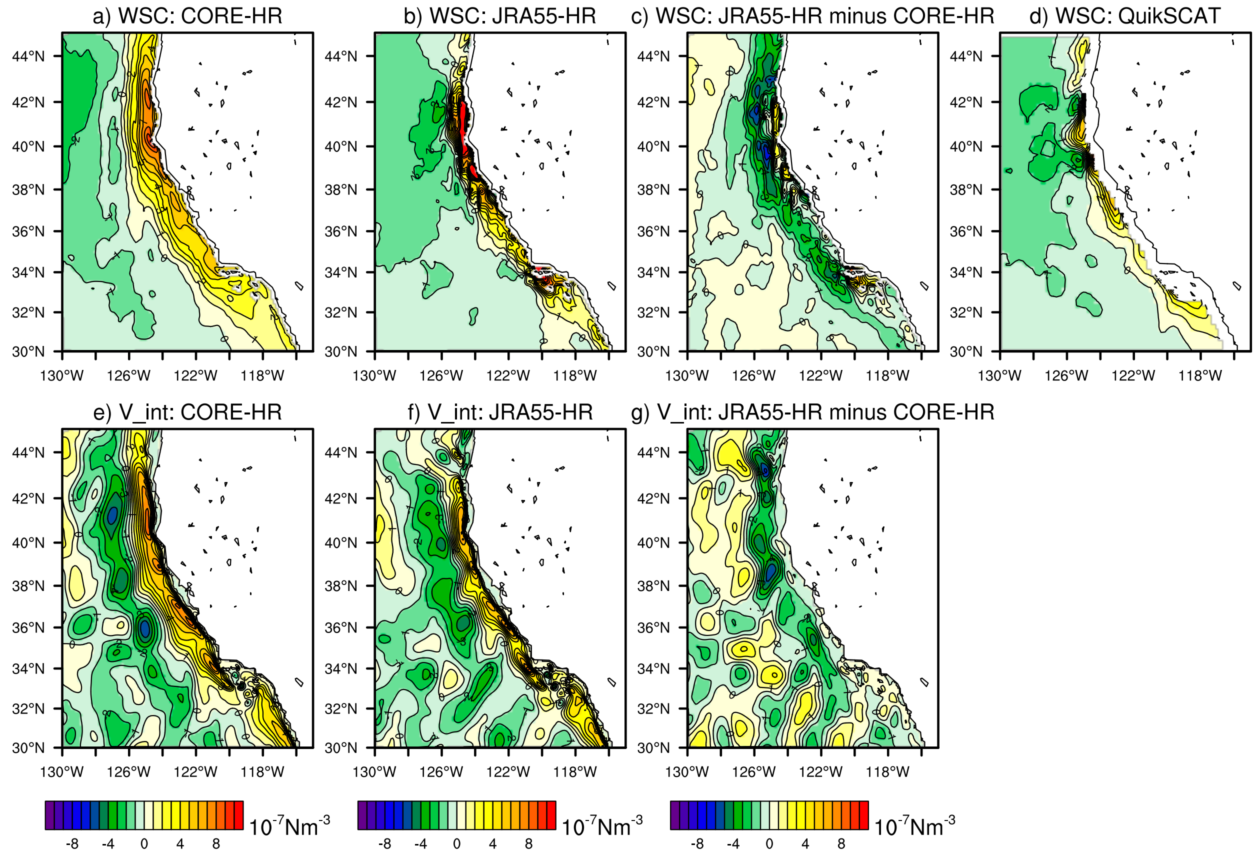

FIG. 11. (a)–(d) Wind stress curl and (e)–(g) $\overline{V}$ in the California Current region in JJA, all from the 0.1° simulations forced by CORE and JRA55-do. Intermodel differences are shown in (c) and (g). Observed wind stress curl from QuikSCAT is shown in (d). All panels use the same color bar. Model results are 2000–09 means.

[as discussed in, e.g., Marchesiello et al. (2003) and Chen et al. (2021)] but still has some influence of WSC. This point will be revisited in section 6 for the Benguela.

The changes to surface stress and WSC also affect the vertical velocity field. Under CORE forcing, the core of the atmosphere jet is located farther offshore, and the WSC pattern induces upward velocity via Ekman pumping w_E (1), so that differences in w_E between simulations at a given latitude are approximately proportional to differences in WSC. Specifically, from the WSC patterns of Figs. 11a–c, we should see that JRA55-do simulations have stronger upward motion than CORE-forced very close to the coast, but weaker vertical motion in a band about 2° wide to the west. Further, from section 1c, the coastally confined upwelling should occur within a few tens of kilometers (a few grid cells of the high-resolution model) and be stronger when forced by JRA55-do's stronger alongshore coastal wind stress. The actual model vertical velocities confirm this prediction: the upwelling close to the coast is enhanced under JRA55-do, but further offshore it is reduced (Figs. 12a,b). The effect is more dramatic for the high-resolution ocean, where vertical velocities at the coast reach upward of 2 m day^{-1} in JRA55-HR and are much stronger than for CORE-HR (Figs. 12c,d). The high-resolution ocean model partly resolves the upwelling-front scale of $O(10)$ km, which is not resolved by the 1° model. [The distance away from the coast where the oceanic coastal jet and coastal upwelling are active has been estimated as between $R_1/2$ and R_1, where R_1 is the first internal Rossby radius of a few tens of kilometers (e.g., Allen 1973; Bordbar et al. 2021).] A further discussion of the relative roles of WSC-driven upwelling and coastal upwelling can be found in Bordbar et al. (2021), where it was seen that the assumption of Ekman pumping combined with coastal Ekman divergence and upwelling worked well for long-term-mean vertical motion, but did not predict the variability [see also Chelton et al. (2007), who found that Ekman pumping anomalies forced by mesoscale eddies were much larger than the mean Ekman pumping forced by the mean winds].

b. *Processes in other regions*

Further inspection of the ocean model state and wind stress forcing for the FOSI simulations revealed a common story of improvement when using JRA55-do for the California Current System and the Peru–Chile and Benguela systems (see supplemental material document "All Regions"). Specifically, stronger wind stress close to the coast in JRA55-do leads to more coastal upwelling and downwind surface ocean flow

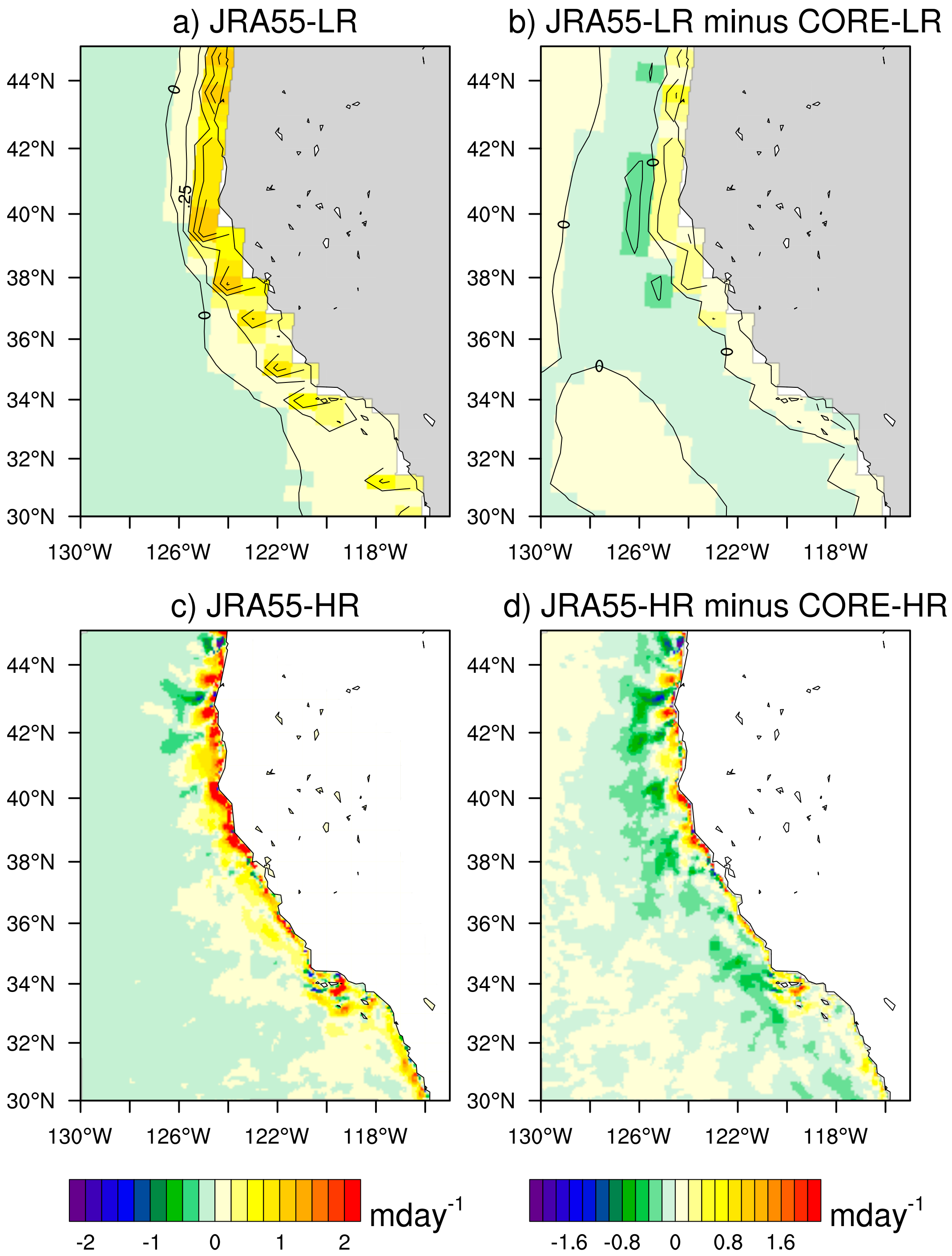
a) JRA55-LR
b) JRA55-LR minus CORE-LR
c) JRA55-HR
d) JRA55-HR minus CORE-HR
44°N
42°N
40°N
38°N
36°N
34°N
32°N
30°N
130°W
126°W
122°W
118°W
25
mday^{-1}
-2
-1
0
1
2
-1.6
-0.8
0
0.8
1.6

FIG. 12. California Current vertical velocity at 50 m. Seasonal JJA average from a 10-yr (2000–09) segment for a (a),(b) 1° ocean model and (c),(d) 0.1° model, (left) using JRA55-do and (right) showing JRA55-do minus CORE. In (a) and (b) the color shading shows individual model grid cells while the line contours have been spatially smoothed. The color bar for each column is displayed at the bottom.

(i.e., the oceanic coastal jet), and meanwhile a narrowing (and shifting) of WSC lead to less poleward flow throughout the water column. Further, the Ekman pumping signal under CORE, which gives rise to too much offshore upwelling, is reduced in JRA55-do. These factors combine to lead to a reduction of the high SST bias when using JRA55-do. The results are consistent with Bonino et al. (2019b), who compared JRA55-do with the coarser-resolution ERA-Interim.

The northwest Africa upwelling is unique in that the sensitivity to ocean resolution is stronger than sensitivity to forcing dataset (Fig. 2), and this appears to be due to the stronger coastal current (and upwelling) with high ocean resolution (Fig. S10), and possibly also due to less sensitivity to WSC (Fig. S11; see also section 7). Off the Benguela, improvements due to changing forcing dataset occur, but these do not seem to be sufficient to counter the combined problem of too much WSC-driven poleward flow and too weak equatorward oceanic coastal jet, which dominate the SST bias, as discussed in detail in the following section.

6. Regional Benguela simulations

Historically, climate models have had more difficulty in simulating upwelling in the Benguela system than in other EBUS (Small et al. 2015; Bonino et al. 2019a; K21) and the results of section 3 show that this is also true of the FOSI experiments of this paper. The Benguela and ABFZ are challenging environments to model, with a detailed spatial structure of the wind field (Patricola and Chang 2017) and a sharp boundary between very different water masses at the ABFZ (Mohrholz et al. 2001) being important features. In observations and model (Fig. 6e), large SST anomalies occur during Benguela Niño events which relate to forcing by changes in local wind stress (e.g., Richter et al. 2010) or remotely forced CTWs (e.g., Koungue et al. 2019), or a combination of the two factors (Koungue et al. 2021). The CTWs can then lead to advection of warm tropical water across the ABFZ (Mohrholz et al. 2001; Rouault et al. 2007, 2012; Koungue et al. 2019), which will lead to large SST anomalies. A relevant question is whether processes leading to transient high SST events in Benguela Niños can also affect the time-mean model bias of SST. Toniazzo and Woolnough (2014) argue that this is possible, with errors in equatorial winds leading to CTWs, which lower the thermocline and lead to higher SST. Here we propose that local wind forcing is also important for the bias, leading to warming via southward transport across the ABFZ.

For this regional investigation, focused regional ocean-only simulations from ROMS were run at 9-km grid spacing. K21 discussed two such sets of simulations (named here ROMS-WRF and ROMS-CORE; see Table 1): as the limitations of the CORE dataset for upwelling in ROMS have already been discussed in detail in K21, this section will instead focus on an additional JRA55-do run (ROMS-JRA55; Table 1) and compare against the ROMS-WRF benchmark run, which provided strong upwelling and minimal SST bias (WRF was run at 27 km to provide forcing; Patricola and Chang 2017).

We first draw attention to the fact that the coastal SST bias in ROMS -JRA55 (Fig. 13b) is similar to (but not identical to, and slightly weaker than) that seen in the global FOSI simulations (Fig. 2i), which gives confidence in using ROMS to interpret the global model results. In the regional Benguela simulations, forcing by JRA55-do gives rise to an annual mean SST bias of 2°–3°C relative to OISST (Fig. 13b), contrasting with the SST bias of less than 1°C in the ROMS-WRF simulation, with no large coastal enhancement and indeed hints of bias reduction along the coast (Fig. 13c).

Comparison of meridional wind stress from the regional simulations with QuikSCAT estimates (Risien and Chelton 2008) reveals two important features: (i) the ROMS-WRF case has a much stronger absolute wind stress at Cape Frio (~17°S) than QuikSCAT, by up to 0.05 N m^{-2} (Figs. 13d,f), also much stronger than in the ROMS-JRA55 case (Fig. 13e), and (ii) the ROMS-WRF case (Fig. 13f) has a less-rapid drop-off of wind stress as the coast is approached than in ROMS-JRA55 (Fig. 13e). Both these features will give rise to higher SST in the JRA55-do case, for the reasons discussed in sections 1c and 5a. Indeed, in sensitivity experiments K21 found that entirely removing the enhanced wind jet off Cape Frio led to a higher SST locally, by around 1°–2°C, while Small et al. (2015) found that a strong wind drop-off led to warming of 2°–3°C in the coastal strip.

Part of the reason for high wind stress in the ROMS-WRF simulation is the use of the COARE3.0 surface flux algorithm (Fairall et al. 2003). As explained in Risien and Chelton (2008), COARE3.0 gives surface stress values a factor of ~1.15 greater than those obtained from Large and Yeager (2004, 2009) for a given input 10-m wind speed. Recall that the Large and Yeager (2004, 2009) algorithm is used for the POP FOSI simulations, while the Risien and Chelton (2008) QuikSCAT product (SCOW) uses the very similar Large et al. (1994; see their appendix A) algorithm. Thus the ROMS-JRA55 simulation is forced by wind stress that is 1.15 times stronger than the JRA55-LR and JRA55-HR simulations of sections 3–5. This may explain why the SST bias under JRA55-do forcing is slightly larger in the FOSI case compared to that using ROMS (as described above). The 1.15 factor also explains why the wind stress in the ROMS simulation forced by JRA55-do is slightly stronger than QuikSCAT (Figs. 13d,e) despite JRA55-do winds being adjusted toward QuikSCAT.

The ocean response to the winds in WRF and JRA55-do forcing is displayed in Fig. 14. ROMS-WRF has a strong coastal ocean oceanic coastal jet (northward flow along the coast from 27° to ~18°S; Fig. 14d), and depth-averaged meridional flow that is also positive along this coast at these latitudes (but exhibiting southward flow farther offshore; Fig. 14e). The WSC field in ROMS-WRF (Fig. 14f) is mostly negative along the eastern boundary but has a region of positive WSC at 17°S (Cape Frio) and very weak negative WSC at 26°S (Luderitz upwelling). These structural details are also seen in QuikSCAT (Fig. S12). In contrast, ROMS-JRA55 shows overall more southward flow especially close to the coast, both at the surface and in the depth integral (Figs. 14a,b), which is due to the weaker along-coast wind (Figs. 13d–f) and the thicker band of negative WSC (Fig. 14c).

The dominant southward vertically integrated meridional flow in ROMS-JRA55 extends as far south as 28°S (Fig. 14b) which is also the extent of large SST bias (Fig. 13b): K21 confirmed in their heat budget analysis that advection of warm water southward was the leading factor causing SST bias in this suite of simulations. When taking the difference between the ROMS-WRF and ROMS-JRA55 simulations (Fig. S13) it is clear that the much lower SST at the eastern boundary in ROMS-WRF coincides with stronger wind stress (positive

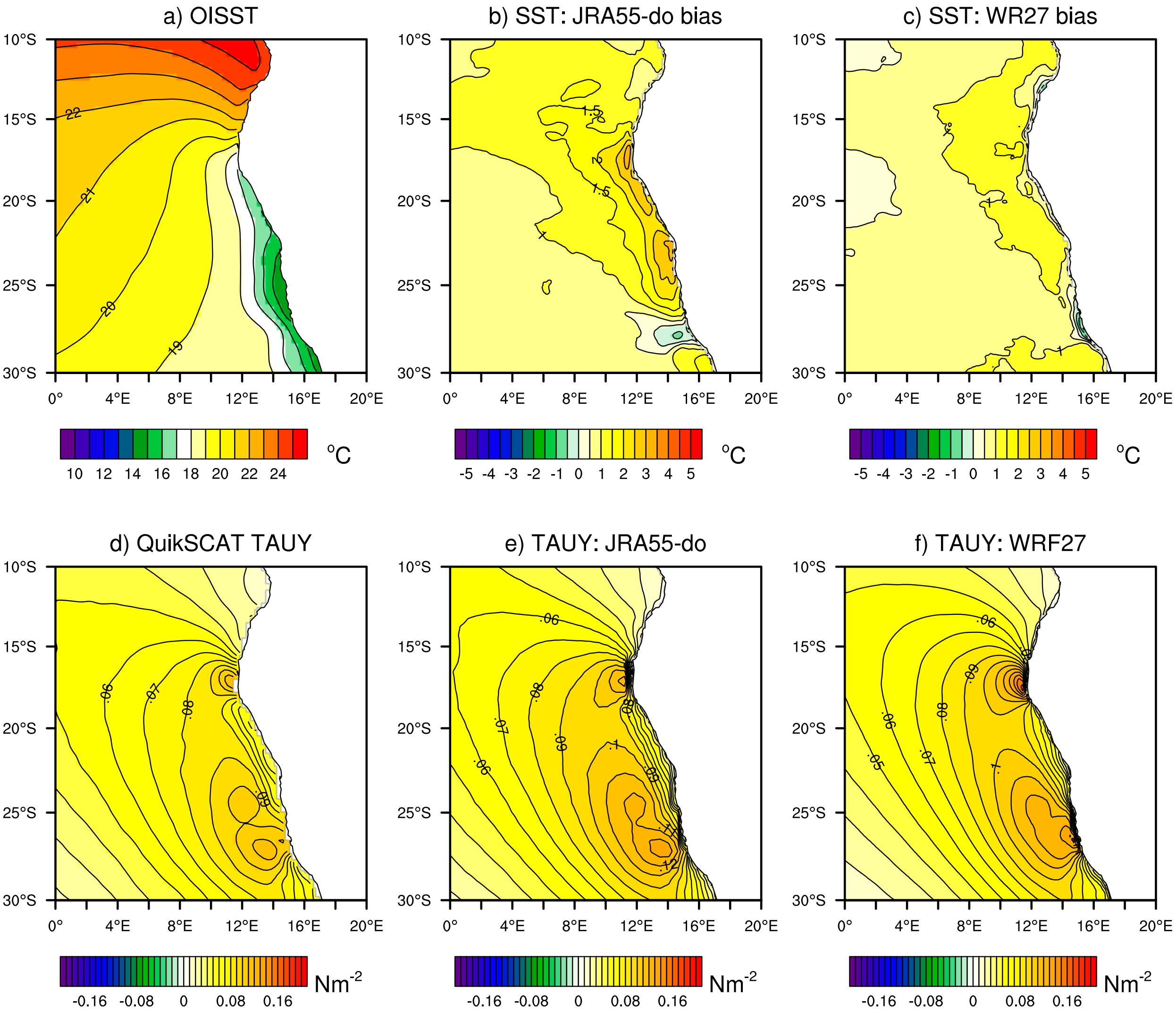
a) OISST
b) SST: JRA55-do bias
c) SST: WR27 bias
d) QuikSCAT TAUY
e) TAUY: JRA55-do
f) TAUY: WRF27

FIG. 13. Regional simulations of the Benguela system. (a) Annual mean SST from Reynolds et al. (2007). (b),(c) SST bias relative to annual mean OISST from ROMS-JRA55 and ROMS-WRF, respectively. Annual mean meridional wind stress from (d) the SCOW product (Risien and Chelton 2008), (e) ROMS-JRA55, and (f) ROMS-WRF.

differences of TAUY), less negative WSC (positive differences of WSC), leading to a stronger northward coastal surface oceanic coastal jet and depth-integrated flow. The vertical velocities are also stronger at the coast in ROMS-WRF than in ROMS-JRA55 (not shown).

In summary, the ROMS-WRF simulation has more realistic SST than ROMS-JRA55 and the global simulations due to the stronger coastal wind stress, reduced wind drop-off, and narrower coastal WSC. A key point is that CORE and JRA55-do-forced cases, both global and regional, are strongly controlled by the WSC whereas the ROMS-WRF case is not (see also K21). When going from the WSC of JRA55-do to that of ROMS-WRF the lateral scale of coastal WSC diminishes rapidly allowing for strong equatorward flow and cold advection to significantly reduce the SST bias, in addition to the influence of stronger coastal upwelling.

Finally, it may be confirmed that the global run JRA55-HR exhibits similar properties to ROMS-JRA55 in terms of the surface and depth-integrated meridional flow and the WSC (Fig. S14), strongly suggesting that the bias in the global run is driven by similar factors to the regional solutions.

7. Discussion

The question of whether the idealized Sverdrup balance [(2)] has any real application to EBUS is of interest. Some evidence for a strong influence of WSC on long-term-averaged and depth-averaged meridional flow has been found by Veitch et al. (2010), Junker et al. (2015), and Siegfried et al. (2019) for the Benguela, and in Penven et al. (2005) for the Peru–Chile system. One term in the barotropic vorticity equation that is neglected in the Sverdrup balance is the bottom

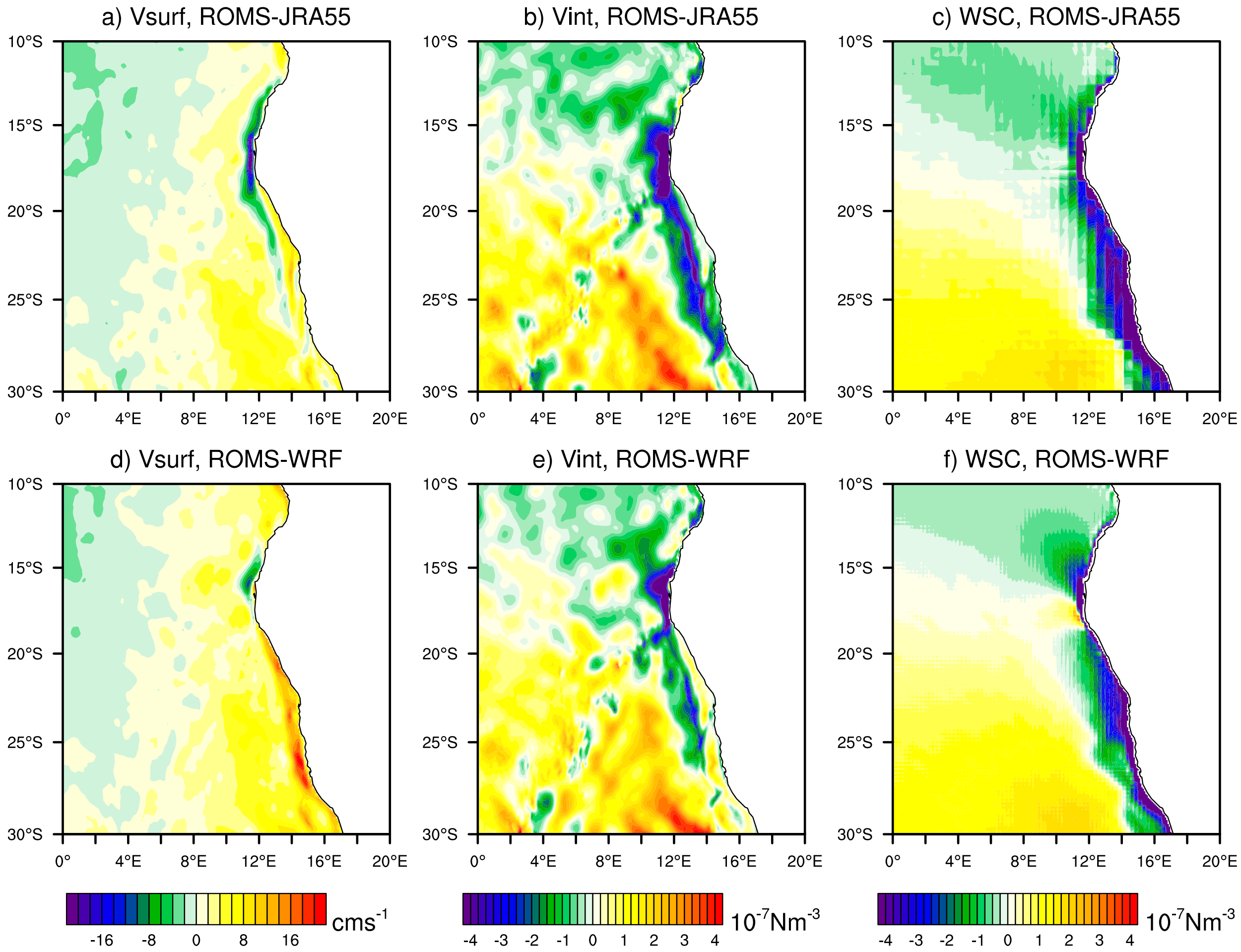

FIG. 14. ROMS meridional velocities (v) and WSC annual mean: (a),(d) v at surface, (b),(e) v integrated to 400-m depth, and (c),(f) WSC for (top) ROMS-JRA55 and (bottom) ROMS-WRF. The color bar for each column is shown at the bottom.

pressure torque (see, e.g., Yeager 2015): in the simulations presented in this paper it was found that this effect had an impact on the coastal flow of interest only in the northwest Africa upwelling, particularly at low resolution, possibly due to the nature of the topography (Fig. S11). Other neglected terms are the nonlinearities in the vorticity equation (e.g., eddy Reynolds stress terms, Marchesiello et al. 2003; Chen et al. 2021), which likely play a significant role in the coastal-eddy-permitting simulations used here (JRA55-HR and CORE-HR), as suggested in Fig. S9.

In the global simulations considered in this paper, many appear to show some features similar to a Sverdrup balance (e.g., Fig. 11), but at the same time they show features characteristic of coastal upwelling. For an illustrative example, Fig. 15 shows WSC and $\overline{V}$ for the Benguela system in JJA, from CORE-HR and JRA55-HR. For both cases, accompanying the negative WSC adjacent to the coast is a band of negative $\overline{V}$ off the coast of similar width and magnitude to that of WSC, which indicates an approximate Sverdrup balance. Does this imply that coastal oceanic jet dynamics are absent in these simulations? To answer this, we consider the vertical dependence of the flow. Figure 16 shows the surface meridional current V_s and the shear from the surface to 100 m ($V_s - V_{100\mathrm{m}}$) for the same cases and season. Whereas both the surface current and the shear are negative in CORE-HR over much of the coastal region (Figs. 16a,c), JRA55-HR exhibits mostly positive surface current and shear, which is strong in a narrow strip adjacent to the coast (Figs. 16b,d). The latter is characteristic of an oceanic coastal jet driven by alongshore wind and confined within a few tens of kilometers (similar scale to the Rossby radius). Returning to Fig. 15, close inspection of $\overline{V}$ near the coast in JRA55-HR shows a similar thin strip of positive values (arrow in Fig. 15d) inshore of the thicker negative band. These results imply that for this case, Sverdrup balance (exact or approximate) does not hold within a few tens of kilometers of the coast, but it is valid, approximately, farther offshore. These results seem consistent with previous work that shows that the eastern subtropical gyre is in approximate Sverdrup balance on long-time averages (Lass and Mohrholz 2008) and also that WSC has an influence on the dynamics of the ABFZ (Colberg and Reason 2006).

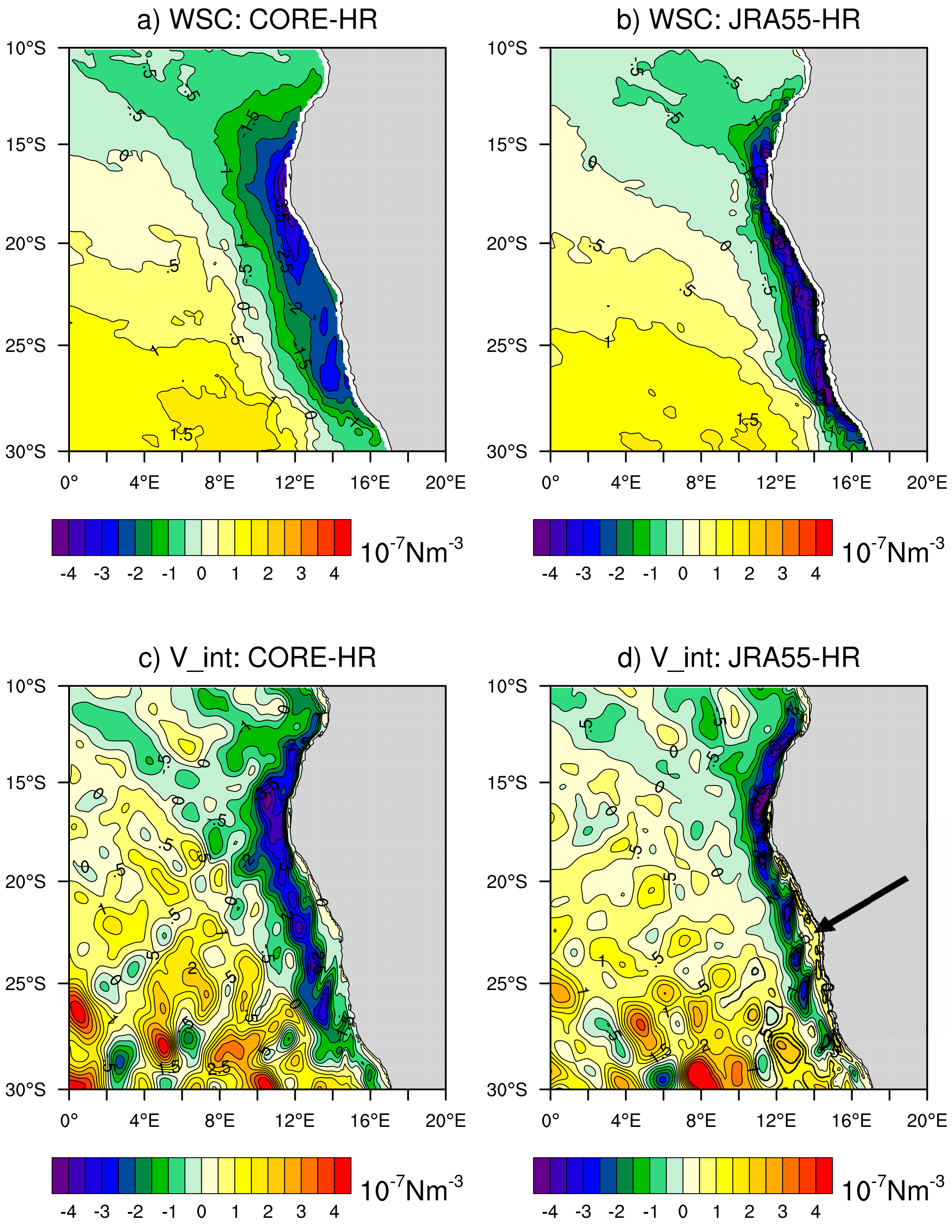
a) WSC: CORE-HR
b) WSC: JRA55-HR
c) V_int: CORE-HR
d) V_int: JRA55-HR
10°S
15°S
20°S
25°S
30°S
0°
4°E
8°E
12°E
16°E
20°E
-4 -3 -2 -1 0 1 2 3 4
$10^{-7}Nm^{-3}$

FIG. 15. (top) WSC and (bottom) depth-integrated meridional velocity in the Benguela/ABFZ in JJA, for (a),(c) CORE-HR and (b),(d) JRA55-HR. The arrow in (d) points to a thin strip of positive velocity next to the coast.

Another point of interest is that the oceanic coastal jet is not necessarily at a maximum where the wind stress is strongest. For example, wind stress has a local maximum at Cape Frio/Kunene (~17°S, Figs. 13d–f), but the oceanic coastal jet in the good ROMS-WRF solution is close to zero at that location (Fig. 14d), and it is negative (upwind) in ROMS-JRA55 (Fig. 14a). This confirms that WSC has an effect even at the surface, as also discussed by Colberg and Reason (2006), and may counteract the downwind oceanic coastal jet effect.

8. Conclusions

The sensitivity of coastal upwelling to forcing dataset and ocean resolution in a forced ocean–sea ice model has been

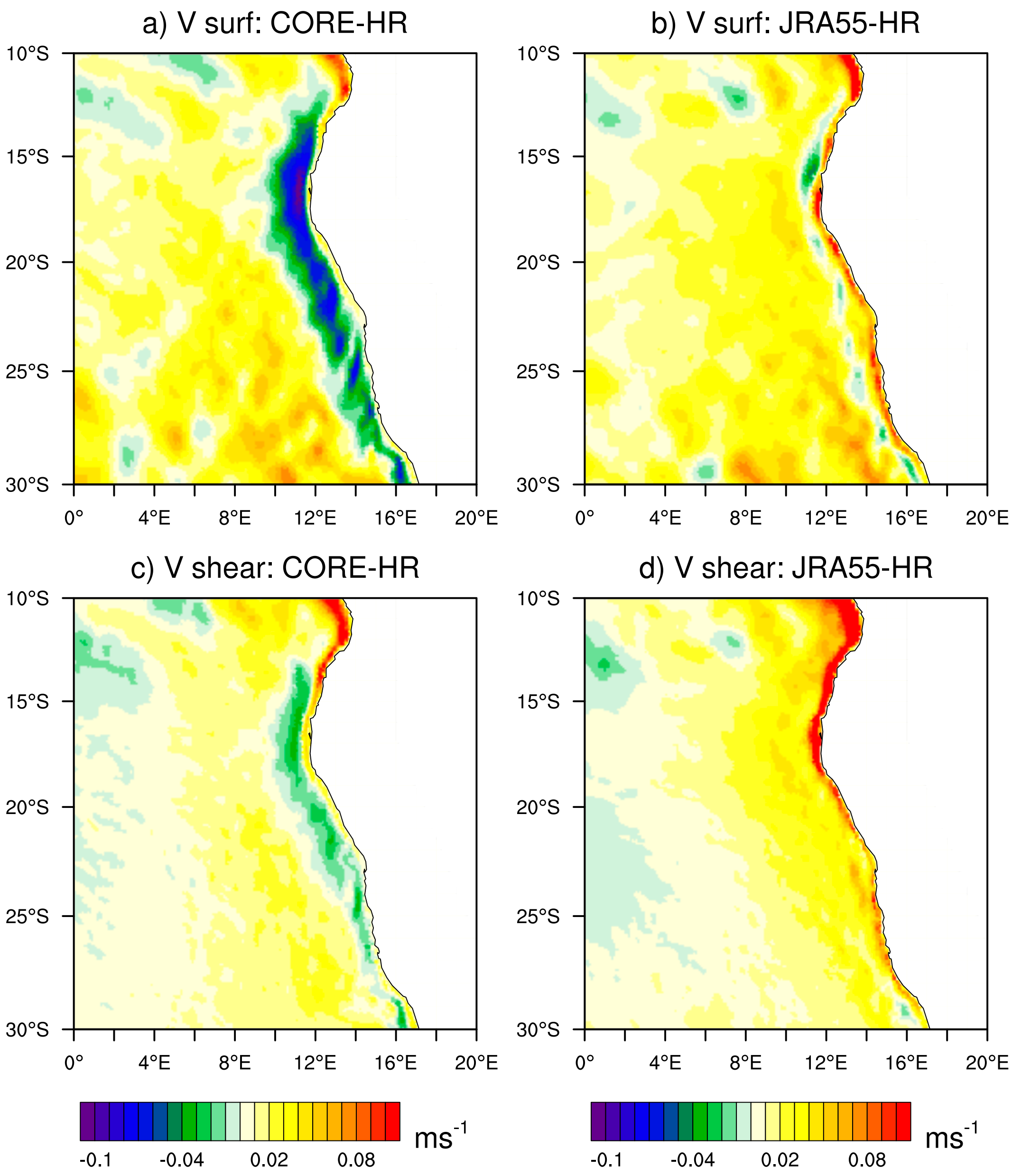

FIG. 16. (top) Surface meridional velocity in JJA and (bottom) associated vertical shear of meridional flow between the surface and 100 m (surface minus 100-m flow) for the Benguela region, for (a),(c) CORE-HR and (b),(d) JRA55-HR. All panels share the same color bar.

explored in multidecadal simulations designed for climate applications. The focus is on SST but related subsurface quantities have also been shown. The hypothesis that much of the SST bias in simulations forced by the coarse-resolution CORE is due to weak alongshore winds, associated with weak downwind surface currents and combined with strong WSC-driven counterflows, is consistent with the presented results. We further show that the problem is corrected in most cases by using the higher-resolution JRA55-do product. However, there are remaining SST biases in the JRA55-do-forced simulations: most notably for the Benguela, but also to a lesser extent for the northwest Africa upwelling and Peru upwellings which still exhibit high SST biases even with a high-resolution ocean grid. (See supplemental text part S4 for a summary of each region.)

Next the implications of mean state bias for monthly-to-interannual variability in upwelling systems were examined. In general, good agreement was found in SST variability between the models and observations. Major factors influencing SST on monthly and longer time scales include teleconnections from the tropics, and long marine heat waves, especially for the California, Peru, and Chile upwelling systems, while the Benguela Niño affected the ABFZ and Benguela domain. Correlations of monthly SST variability between model and observations were overall highest with JRA55-do forcing, and the regions with lowest correlations were the Benguela and ABFZ, suggesting that for those regions alone processes affecting the large mean state bias might also influence variability. The variability of SSH and of upwelling velocity were also examined and the results were consistent with those for SST.

Finally, the question was addressed of how appropriate is idealized Sverdrup balance in these coastal upwelling systems? It was shown that Sverdrup balance has some utility in explaining long-term average differences of meridional flow between simulations that have different WSC. However, it misses important processes like bottom torque (most relevant here off northwest Africa), eddy stresses, and the downwind oceanic coastal jet. We thus found that off California, the depth-averaged poleward flow in JRA55-HR was not well predicted by Sverdrup balance except in a specific region (beyond a few tens of kilometers off the coast and extending to 2°–3° of longitude away from the coast). Meanwhile in the Benguela, Sverdrup balance applied well in the global model simulations outside of a few tens of kilometers off the coast; however, within that narrow band close to the coast, the depth-averaged meridional flow in JRA55-HR (and in ROMS-WRF; K21) was equatorward and of opposite sign to the WSC, due to the oceanic coastal jet.

Acknowledgments. The editors and three anonymous reviewers are thanked for their comments which helped improve the manuscript. JRA55-do was produced by the Meteorological Research Institute of the JMA, with funding from JSPS KAKENHI Grant 15H03726 and supported by NOAA CPO CVP. One cycle of the JRA55-do forcing of high-resolution POP/CICE was performed on the Cheyenne supercomputer. Computing and data storage resources, including the Cheyenne supercomputer (https://doi.org/10.5065/D6RX99HX), were provided by the Computational and Information Systems Laboratory (CISL) at NSF NCAR. The remaining three of the four cycles were performed under the International Laboratory for High Resolution Earth System Prediction, a collaboration between QNLM, China, Texas A&M, and NSF NCAR. The simulations were run on the Frontera platform at the Texas Advanced Computing Center. The high-resolution CORE simulation was performed by Ben Johnson, who is gratefully acknowledged. OISST was gathered from https://www.ncei.noaa.gov/data/sea-surface-temperature-optimum-interpolation/. Sea surface height (SSH) anomalies are obtained from CMEMS at https://data.marine.copernicus.eu/product/SEALEVEL_GLO_PHY_L4_MY_008_047/services. Niño-3.4 data were gathered from NOAA ESRL https://psl.noaa.gov/data/correlation/nina34.data and are based on ersstv5. Niño1 + 2 data are from https://psl.noaa.gov/data/correlation/nina1.data. The CUTI of Jacox et al. (2018) (monthly mean) was downloaded from https://mjacox.com/upwelling-indices/ in January 2023. We thank Mike Alexander for providing comments on a draft of this paper. We also acknowledge informative discussions with Dudley Chelton and Guilia Bonino, LuAnne Thompson, and Martin Schmidt. The CESM project is supported primarily by the National Science Foundation (NSF). This material is based upon work supported by NSF National Center for Atmospheric Research, which is a major facility sponsored by the NSF under Cooperative Agreement No. 1852977.

Data availability statement. The data used in this work is available under the Climate Data Gateway at NCAR (https://www.earthsystemgrid.org/) at https://doi.org/10.26024/tp2m-af86. The current CESM2 version is freely available online (at www.cesm.ucar.edu/models/cesm2/).

REFERENCES

Alexander, M. A., I. Bladé, M. Newman, J. R. Lazante, N.-C. Lau, and J. D. Scott, 2002: The atmospheric bridge: The influence of ENSO teleconnections on air–sea interaction over the global oceans. *J. Climate*, **15**, 2205–2231, https://doi.org/10.1175/1520-0442(2002)015<2205:TABTIO>2.0.CO;2.

Allen, J. S., 1973: Upwelling and coastal jets in a continuously stratified ocean. *J. Phys. Oceanogr.*, **3**, 245–257, https://doi.org/10.1175/1520-0485(1973)003<0245:UACJIA>2.0.CO;2.

Amaya, D. J., M. G. Jacox, J. Dias, M. A. Alexander, K. B. Karnauskas, J. D. Scott, and M. Gehne, 2022: Subseasonal-to-seasonal forecast skill in the California Current System and its connection to coastal Kelvin waves. *J. Geophys. Res. Oceans*, **127**, e2021JC017892, https://doi.org/10.1029/2021JC017892.

Bakun, A., 1973: Coastal upwelling indices, West Coast of North America, 1946–71. NOAA Tech. Rep. NMFS SSRF-671, 112 pp., https://spo.nmfs.noaa.gov/SSRF/SSRF671.pdf.

——, 1990: Global climate change and intensification of coastal ocean upwelling. *Science*, **247**, 198–200, https://doi.org/10.1126/science.247.4939.198.

Banzon, V. F., R. W. Reynolds, D. Stokes, and Y. Xue, 2014: A 1/4°-spatial-resolution daily sea surface temperature climatology based on a blended satellite and in situ analysis. *J. Climate*, **27**, 8221–8228, https://doi.org/10.1175/JCLI-D-14-00293.1.

Bograd, S. J., and Coauthors, 2023: Climate change impacts on eastern boundary upwelling systems. *Annu. Rev. Mar. Sci.*, **15**, 303–328, https://doi.org/10.1146/annurev-marine-032122-021945.

Bond, N. A., M. F. Cronin, H. Freeland, and N. Mantua, 2015: Causes and impacts of the 2014 warm anomaly in the NE Pacific. *Geophys. Res. Lett.*, **42**, 3414–3420, https://doi.org/10.1002/2015GL063306.

Bonino, G., E. Di Lorenzo, S. Masina, and D. Iovino, 2019a: Interannual to decadal variability within and across the major eastern boundary upwelling systems. *Sci. Rep.*, **9**, 19949, https://doi.org/10.1038/s41598-019-56514-8.

——, S. Masina, D. Iovino, A. Storto, and H. Tsujino, 2019b: Eastern boundary upwelling systems response to different atmospheric forcing in a global eddy-permitting ocean model. *J. Mar. Syst.*, **197**, 103178, https://doi.org/10.1016/j.jmarsys.2019.05.004.

Bordbar, M. H., V. Mohrholz, and M. Schmidt, 2021: The relation of wind-driven coastal and offshore upwelling in the Benguela upwelling system. *J. Phys. Oceanogr.*, **51**, 3117–3133, https://doi.org/10.1175/JPO-D-20-0297.1.

Brady, R. X., M. A. Alexander, N. S. Lovenduski, and R. R. Rykaczewski, 2017: Emergent anthropogenic trends in California Current upwelling. *Geophys. Res. Lett.*, **44**, 5044–5052, https://doi.org/10.1002/2017GL072945.

Brink, K. H., 1983: The near-surface dynamics of coastal upwelling. *Prog. Oceanogr.*, **12**, 223–257, https://doi.org/10.1016/0079-6611(83)90009-5.

Bryan, F. O., and S. Bachman, 2015: Isohaline salinity budget of the North Atlantic salinity maximum. *J. Phys. Oceanogr.*, **45**, 724–736, https://doi.org/10.1175/JPO-D-14-0172.1.

Capet, X. J., P. Marchesiello, and J. C. McWilliams, 2004: Upwelling response to coastal wind profiles. *Geophys. Res. Lett.*, **31**, L13311, https://doi.org/10.1029/2004GL020123.

Chang, P., and Coauthors, 2020: An unprecedented set of high-resolution climate simulations from the International Laboratory for High-Resolution Earth System Prediction (iHESP). *2020 Fall Meeting*, Online, Amer. Geophys. Union, Abstract #A097-01.

——, and Coauthors, 2023: Uncertain future of sustainable fisheries environment in eastern boundary upwelling zones under climate change. *Commun. Earth Environ.*, **4**, 19, https://doi.org/10.1038/s43247-023-00681-0.

Chapman, D. C., 1985: Numerical treatment of cross-shelf open boundaries in a barotropic coastal ocean model. *J. Phys. Oceanogr.*, **15**, 1060–1075, https://doi.org/10.1175/1520-0485(1985)015<1060:NTOCSO>2.0.CO;2.

Charney, J. G., 1955: Generation of oceanic currents by wind. *J. Mar. Res.*, **14**, 477–498.

Chassignet, E. P., and Coauthors, 2020: Impact of horizontal resolution on global ocean-sea-ice model simulations based on the experimental protocols of the Ocean Model Intercomparison Project phase 2 (OMIP-2). *Geosci. Model Dev.*, **13**, 4595–4637, https://doi.org/10.5194/gmd-13-4595-2020.

Chavez, F. P., and M. Messie, 2009: A comparison of eastern boundary upwelling systems. *Prog. Oceanogr.*, **83**, 80–96, https://doi.org/10.1016/j.pocean.2009.07.032.

Chelton, D. B., and R. E. Davis, 1982: Monthly mean sea-level variability along the West Coast of North America. *J. Phys. Oceanogr.*, **12**, 757–784, https://doi.org/10.1175/1520-0485(1982)012<0757:MMSLVA>2.0.CO;2.

——, M. G. Schlax, and R. M. Samelson, 2007: Summertime coupling between sea surface temperature and wind stress in the California Current System. *J. Phys. Oceanogr.*, **37**, 495–517, https://doi.org/10.1175/JPO3025.1.

Chen, R., J. C. McWilliams, and L. Renault, 2021: Momentum governors of the California Undercurrent transport. *J. Phys. Oceanogr.*, **51**, 2915–2932, https://doi.org/10.1175/JPO-D-20-0234.1.

Colas, F., X. Capet, J. C. McWilliams, and A. Shchepetkin, 2008: 1997–1998 El Niño off Peru: A numerical study. *Prog. Oceanogr.*, **79**, 138–155, https://doi.org/10.1016/j.pocean.2008.10.015.

Colberg, F., and C. J. C. Reason, 2006: A model study of the Angola Benguela Frontal Zone: Sensitivity to atmospheric forcing. *Geophys. Res. Lett.*, **33**, L19608, https://doi.org/10.1029/2006GL027463.

Connolly, T. P., B. M. Hickey, I. Shulman, and R. E. Thomson, 2014: Coastal trapped waves, alongshore pressure gradients, and the California Undercurrent. *J. Phys. Oceanogr.*, **44**, 319–342, https://doi.org/10.1175/JPO-D-13-095.1.

Danabasoglu, G., W. G. Large, and B. P. Briegleb, 2010: Climate impacts of parameterized Nordic Sea overflows. *J. Geophys. Res.*, **115**, C11005, https://doi.org/10.1029/2010JC006243.

——, S. C. Bates, B. P. Briegleb, S. R. Jayne, M. Jochum, W. G. Large, S. Peacock, and S. G. Yeager, 2012: The CCSM4 ocean component. *J. Climate*, **25**, 1361–1389, https://doi.org/10.1175/JCLI-D-11-00091.1.

——, and Coauthors, 2014: North Atlantic simulations in Coordinated Ocean-ice Reference Experiments phase II (CORE-II). Part I: Mean states. *Ocean Modell.*, **73**, 76–107, https://doi.org/10.1016/j.ocemod.2013.10.005.

——, and Coauthors, 2020: Community Earth System Model version 2 (CESM2). *J. Adv. Model. Earth Syst.*, **12**, e2019MS001916, https://doi.org/10.1029/2019MS001916.

Deppenmeier, A. L., and Coauthors, 2020: The effect of vertical ocean mixing on the tropical Atlantic in a coupled global climate model. *Climate Dyn.*, **54**, 5089–5109, https://doi.org/10.1007/s00382-020-05270-x.

de Szoeke, S. P., C. W. Fairall, D. E. Wolfe, L. Bariteau, and P. Zuidema, 2010: Surface flux observations on the southeastern tropical Pacific Ocean and attribution of SST errors in coupled ocean-atmosphere models. *J. Climate*, **23**, 4152–4174, https://doi.org/10.1175/2010JCLI3411.1.

Di Lorenzo, E., and N. Mantua, 2016: Multi-year persistence of the 2014/15 North Pacific marine heatwave. *Nat. Climate Change*, **6**, 1042–1047, https://doi.org/10.1038/nclimate3082.

Ding, H., M. A. Alexander, and M. G. Jacox, 2021: Role of geostrophic currents in future changes of coastal upwelling in the California Current System. *Geophys. Res. Lett.*, **48**, e2020GL090768, https://doi.org/10.1029/2020GL090768.

Dorman, C. E., and D. Koračin, 2008: Response of the summer marine layer flow to an extreme California Coastal Bend. *Mon. Wea. Rev.*, **136**, 2894–2922, https://doi.org/10.1175/2007MWR2336.1.

Ducet, N., P. Y. Le Traon, and G. Reverdin, 2000: Global high resolution mapping of ocean circulation from the combination of TOPEX/Poseidon and ERS-1 and 2. *J. Geophys. Res.*, **105**, 19 477–19 498, https://doi.org/10.1029/2000JC900063.

Emery, W. J., and K. Hamilton, 1985: Atmospheric forcing of interannual variability in the northeast Pacific Ocean: Connections with El Niño. *J. Geophys. Res.*, **90**, 857–868, https://doi.org/10.1029/JC090iC01p00857.

Enfield, D. B., and J. S. Allen, 1980: On the structure and dynamics of monthly sea level anomalies along the Pacific coast of North and South America. *J. Phys. Oceanogr.*, **10**, 557–578, https://doi.org/10.1175/1520-0485(1980)010<0557:OTSADO>2.0.CO;2.

Fairall, C. W., E. F. Bradley, J. E. Hare, A. A. Grachev, and J. B. Edson, 2003: Bulk parameterization of air–sea fluxes: Updates and verification for the COARE algorithm. *J. Climate*, **16**, 571–591, https://doi.org/10.1175/1520-0442(2003)016<0571:BPOASF>2.0.CO;2.

Fennel, W., and H. U. Lass, 2007: On the impact of wind curls on coastal currents. *J. Mar. Syst.*, **68**, 128–142, https://doi.org/10.1016/j.jmarsys.2006.11.004.

——, T. Junker, M. Schmidt, and V. Mohrholz, 2012: Response of the Benguela upwelling systems to spatial variations in the wind stress. *Cont. Shelf Res.*, **45**, 65–77, https://doi.org/10.1016/j.csr.2012.06.004.

Flather, R. A., 1976: A tidal model of the northwest European continental shelf. *Mém. Soc. Roy. Sci. Liège*, **10**, 141–164.

Florenchie, P. J., R. E. Lutjeharms, C. J. C. Reason, S. Masson, and M. Rouault, 2003: The source of Benguela Niños in the South Atlantic Ocean. *Geophys. Res. Lett.*, **30**, 1505, https://doi.org/10.1029/2003GL017172.

Fox-Kemper, B., R. Ferrari, and R. Hallberg, 2008: Parameterization of mixed layer eddies. Part I: Theory and diagnosis. *J. Phys. Oceanogr.*, **38**, 1145–1165, https://doi.org/10.1175/2007JPO3792.1.

Frischknecht, M., M. Münnich, and N. Gruber, 2015: Remote versus local influence of ENSO on the California Current System. *J. Geophys. Res. Oceans*, **120**, 1353–1374, https://doi.org/10.1002/2014JC010531.

Fu, D., and Coauthors, 2021: Introducing the new Regional Community Earth System Model, R-CESM. *Bull. Amer. Meteor. Soc.*, **102**, E1821–E1843, https://doi.org/10.1175/BAMS-D-20-0024.1.

García-Reyes, M., W. J. Sydeman, D. S. Schoeman, R. R. Rykaczewski, B. A. Black, A. J. Smit, and S. J. Bograd, 2015: Under pressure: Climate change, upwelling, and eastern boundary upwelling ecosystems. *Front. Mar. Sci.*, **2**, 109, https://doi.org/10.3389/fmars.2015.00109.

Garreaud, R. D., and R. C. Munoz, 2005: The low-level jet off the west coast of subtropical South America: Structure and variability. *Mon. Wea. Rev.*, **133**, 2246–2261, https://doi.org/10.1175/MWR2972.1.

Gay, P. S., and T. K. Chereskin, 2009: Mean structure and seasonal variability of the poleward undercurrent off Southern California. *J. Geophys. Res.*, **114**, C02007, https://doi.org/10.1029/2008JC004886.

Gent, P. R., and J. C. McWilliams, 1990: Isopycnal mixing in ocean circulation models. *J. Phys. Oceanogr.*, **20**, 150–155, https://doi.org/10.1175/1520-0485(1990)020<0150:IMIOCM>2.0.CO;2.

——, S. G. Yeager, R. B. Neale, S. Levis, and D. A. Bailey, 2010: Improvements in a half degree atmosphere/land version of the CCSM. *Climate Dyn.*, **34**, 819–833, https://doi.org/10.1007/s00382-009-0614-8.

Gentemann, C. L., M. R. Fewings, and M. García-Reyes, 2017: Satellite sea surface temperatures along the West Coast of the United States during the 2014–2016 Northeast Pacific marine heat wave. *Geophys. Res. Lett.*, **44**, 312–319, https://doi.org/10.1002/2016GL071039.

Goubanova, K., E. Sanchez-Gomez, C. Frauen, and A. Voldoire, 2019: Respective roles of remote and local wind stress forcings in the development of warm SST errors in the south-eastern tropical Atlantic in a coupled high-resolution model. *Climate Dyn.*, **52**, 1359–1382, https://doi.org/10.1007/s00382-018-4197-0.

Griffies, S. M., and Coauthors, 2009: Coordinated Ocean-ice Reference Experiments (COREs). *Ocean Modell.*, **26** (1–2), 1–46, https://doi.org/10.1016/j.ocemod.2008.08.007.

Grodsky, S. A., J. A. Carton, S. Nigam, and Y. M. Okumura, 2012: Tropical Atlantic biases in CCSM4. *J. Climate*, **25**, 3684–3701, https://doi.org/10.1175/JCLI-D-11-00315.1.

Haidvogel, D. B., and Coauthors, 2008: Ocean forecasting in terrain-following coordinates: Formulation and skill assessment of the regional ocean modeling system. *J. Comput. Phys.*, **227**, 3595–3624, https://doi.org/10.1016/j.jcp.2007.06.016.

Hartmann, D. L., 2015: Pacific sea surface temperature and the winter of 2014. *Geophys. Res. Lett.*, **42**, 1894–1902, https://doi.org/10.1002/2015GL063083.

Hickey, B. M., and N. E. Pola, 1983: The seasonal alongshore pressure gradient on the West Coast of the United States. *J. Geophys. Res.*, **88**, 7623–7633, https://doi.org/10.1029/JC088iC12p07623.

Hunke, E. C., W. H. Lipscomb, A. K. Turner, N. Jeffery, and S. Elliott, 2015: CICE: The Los Alamos Sea ice model documentation and software user's manual, version 5.1. Tech. Rep. LA-CC-06-012, 116 pp.

Huyer, A., P. A. Wheeler, P. T. Strub, R. L. Smith, R. Letelier, and P. M. Kosro, 2007: The Newport line off Oregon—Studies in the North East Pacific. *Prog. Oceanogr.*, **75**, 126–160, https://doi.org/10.1016/j.pocean.2007.08.003.

Illig, S., and M.-L. Bachèlery, 2019: Propagation of subseasonal equatorially-forced coastal trapped waves down to the Benguela upwelling system. *Sci. Rep.*, **9**, 5306, https://doi.org/10.1038/s41598-019-41847-1.

Jacox, M. G., C. A. Edwards, E. L. Hazen, and S. J. Bograd, 2018: Coastal upwelling revisited: Ekman, Bakun, and improved upwelling indices for the U.S. West Coast. *J. Geophys. Res.*, **123**, 7332–7350, https://doi.org/10.1029/2018JC014187.

——, M. A. Alexander, C. A. Stock, and G. Hervieux, 2019: On the skill of seasonal sea surface temperature forecasts in the California Current System and its connection to ENSO variability. *Climate Dyn.*, **53**, 7519–7533, https://doi.org/10.1007/s00382-017-3608-y.

Johnson, B. K., F. O. Bryan, S. A. Grodsky, and J. A. Carton, 2016: Climatological annual cycle of the salinity budgets of the subtropical maxima. *J. Phys. Oceanogr.*, **46**, 2981–2994, https://doi.org/10.1175/JPO-D-15-0202.1.

Junker, T., M. Schmidt, and V. Mohrholz, 2015: The relation of wind stress curl and meridional transport in the Benguela upwelling system. *J. Mar. Syst.*, **143**, 1–6, https://doi.org/10.1016/j.jmarsys.2014.10.006.

Kara, A. B., A. J. Wallcraft, and H. E. Hurlbert, 2007: A correction for land contamination of atmospheric variables near land–sea boundaries. *J. Phys. Oceanogr.*, **37**, 803–818, https://doi.org/10.1175/JPO2984.1.

Kobayashi, S., and Coauthors, 2015: The JRA-55 reanalysis: General specifications and basic characteristics. *J. Meteor. Soc. Japan*, **93**, 5–48, https://doi.org/10.2151/jmsj.2015-001.

Koungue, R. A. I., M. Rouault, S. Illig, P. Brandt, and J. Jouanno, 2019: Benguela Niños and Benguela Niñas in forced ocean simulation from 1958 to 2015. *J. Geophys. Res. Oceans*, **124**, 5923–5951, https://doi.org/10.1029/2019JC015013.

——, P. Brandt, J. Lübbecke, A. Prigent, M. S. Martins, and R. R. Rodrigues, 2021: The 2019 Benguela Niño. *Front. Mar. Sci.*, **8**, 800103, https://doi.org/10.3389/fmars.2021.800103.

Kurian, J., P. Li, P. Chang, C. M. Patricola, and J. Small, 2021: Impact of the Benguela coastal low-level jet on the southeast tropical Atlantic SST bias in a regional ocean model. *Climate Dyn.*, **56**, 2773–2800, https://doi.org/10.1007/s00382-020-05616-5.

Large, W. G., and S. G. Yeager, 2004: Diurnal to decadal global forcing for ocean and sea-ice models: The data sets and flux climatologies. NCAR Tech. Note NCAR/TN-460+STR, 105 pp., https://doi.org/10.5065/D6KK98Q6.

——, and G. Danabasoglu, 2006: Attribution and impacts of upper-ocean biases in CCSM3. *J. Climate*, **19**, 2325–2346, https://doi.org/10.1175/JCLI3740.1.

——, and S. G. Yeager, 2009: The global climatology of an interannually varying air-sea flux data set. *Climate Dyn.*, **33**, 341–364, https://doi.org/10.1007/s00382-008-0441-3.

——, and ——, 2012: On the observed trends and changes in global sea surface temperature and air–sea heat fluxes (1984–2006). *J. Climate*, **25**, 6123–6135, https://doi.org/10.1175/JCLI-D-11-00148.1.

——, J. C. McWilliams, and S. C. Doney, 1994: Oceanic vertical mixing: A review and a model with nonlocal boundary layer parameterization. *Rev. Geophys.*, **32**, 363–403, https://doi.org/10.1029/94RG01872.

Lass, H. U., and V. Mohrholz, 2008: On the interaction between the subtropical gyre and the subtropical cell on the shelf of the SE Atlantic. *J. Mar. Syst.*, **74** (1–2), 1–43, https://doi.org/10.1016/j.jmarsys.2007.09.008.

Lellouche, J.-M., and Coauthors, 2021: The Copernicus global 1/12° oceanic and sea ice GLORYS12 reanalysis. *Front. Earth Sci.*, **9**, 698876, https://doi.org/10.3389/feart.2021.698876.

Lemarié, F., J. Kurian, A. F. Shchepetkin, M. J. Molemaker, F. Colas, and J. C. McWilliams, 2012: Are there inescapable issues prohibiting the use of terrain-following coordinates in climate models? *Ocean Modell.*, **42**, 57–79, https://doi.org/10.1016/j.ocemod.2011.11.007.

Lythe, M. B., D. G. Vaughan, and BEDMAP Consortium, 2000: BEDMAP—Bed topography of the Antarctic. 1:10,000,000 scale map. BAS (Misc) 9. British Antarctic Survey.

Ma, C.-C., C. R. Mechoso, A. W. Robertson, and A. Arakawa, 1996: Peruvian stratus clouds and the tropical Pacific circulation: A coupled ocean-atmosphere GCM study. *J. Climate*, **9**, 1635–1645, https://doi.org/10.1175/1520-0442(1996)009<1635:PSCATT>2.0.CO;2.

Marchesiello, P., J. C. McWilliams, and A. Shchepetkin, 2001: Open boundary conditions for long-term integration of regional oceanic models. *Ocean Modell.*, **3** (1–2), 1–20, https://doi.org/10.1016/S1463-5003(00)00013-5.

——, ——, and ——, 2003: Equilibrium structure and dynamics of the California Current System. *J. Phys. Oceanogr.*, **33**, 753–783, https://doi.org/10.1175/1520-0485(2003)33<753:ESADOT>2.0.CO;2.

McCreary, J. P., P. K. Kundu, and S.-Y. Chao, 1987: On the dynamics of the California Current System. *J. Mar. Res.*, **45** (1), 1–32, https://doi.org/10.1357/002224087788400945.

Mohrholz, V., M. Schmidt, J. Lutjeharms, and H.-C. John, 2001: The hydrography and dynamics of the Angola-Benguela frontal zone in April 1999. *S. Afr. J. Sci.*, **97**, 199–208.

——, A. Eggert, T. Junker, G. Nausch, T. Ohde, and M. Schmidt, 2014: Cross shelf hydrographic and hydrochemical conditions and their short-term variability at the Northern Benguela during a normal upwelling season. *J. Mar. Syst.*, **140**, 92–110, https://doi.org/10.1016/j.jmarsys.2014.04.019.

Nicholson, S. E., 2010: A low-level jet along the Benguela coast, an integral part of the Benguela Current ecosystem. *Climatic Change*, **99**, 613–624, https://doi.org/10.1007/s10584-009-9678-z.

Parish, T. R., 2000: Forcing of the summertime low-level jet along the California coast. *J. Appl. Meteor.*, **39**, 2421–2433, https://doi.org/10.1175/1520-0450(2000)039<2421:FOTSLL>2.0.CO;2.

Patricola, C. M., and P. Chang, 2017: Structure and dynamics of the Benguela low-level coastal jet. *Climate Dyn.*, **49**, 2765–2788, https://doi.org/10.1007/s00382-016-3479-7.

Pauly, D., and V. Christensen, 1995: Primary production required to sustain global fisheries. *Nature*, **374**, 255–257, https://doi.org/10.1038/374255a0.

Penven, P., V. Echevin, J. Pasapera, F. Colas, and J. Tam, 2005: Average circulation, seasonal cycle, and mesoscale dynamics of the Peru Current System: A modeling approach. *J. Geophys. Res.*, **110**, C10021, https://doi.org/10.1029/2005JC002945.

Philander, S. G. H., and J.-H. Yoon, 1982: Eastern boundary currents and coastal upwelling. *J. Phys. Oceanogr.*, **12**, 862–879, https://doi.org/10.1175/1520-0485(1982)012<0862:EBCACU>2.0.CO;2.

Pickett, M. H., and J. D. Paduan, 2003: Ekman transport and pumping in the California Current based on the U.S. Navy's high resolution atmospheric model (COAMPS). *J. Geophys. Res.*, **108**, 3327, https://doi.org/10.1029/2003JC001902.

Pozo Buil, M., and Coauthors, 2021: A dynamically downscaled ensemble of future projections for the California Current System. *Front. Mar. Sci.*, **8**, 612874, https://doi.org/10.3389/fmars.2021.612874.

Ramp, S. R., J. L. McClean, C. A. Collins, A. J. Semtner, and K. A. S. Hays, 1997: Observations and modeling of the 1991–1992 El Niño signal off central California. *J. Geophys. Res.*, **102**, 5553–5582, https://doi.org/10.1029/96JC03050.

Reynolds, R. W., T. M. Smith, C. Liu, D. B. Chelton, K. S. Casey, and M. G. Schlax, 2007: Daily high-resolution-blended analyses for sea surface temperature. *J. Climate*, **20**, 5473–5496, https://doi.org/10.1175/2007JCLI1824.1.

——, D. B. Chelton, J. Roberts-Jones, M. J. Martin, D. Menemenlis, and C. J. Merchant, 2013: Objective determination of feature resolution in two sea surface temperature analyses. *J. Climate*, **26**, 2514–2533, https://doi.org/10.1175/JCLI-D-12-00787.1.

Richter, I., 2015: Climate model biases in the eastern tropical oceans: Causes, impacts and ways forward. *Wiley Interdiscip. Rev.: Climate Change*, **6**, 345–358, https://doi.org/10.1002/wcc.338.

——, S. K. Behera, Y. Masumoto, B. Taguchi, N. Komori, and T. Yamagata, 2010: On the triggering of Benguela Niños: Remote equatorial versus local influences. *Geophys. Res. Lett.*, **37**, L20604, https://doi.org/10.1029/2010GL044461.

——, S.-P. Xie, A. T. Wittenberg, and Y. Masumoto, 2012: Tropical Atlantic biases and their relationship to surface wind stress and terrestrial precipitation. *Climate Dyn.*, **38**, 985–1001, https://doi.org/10.1007/s00382-011-1038-9.

Risien, C. M., and D. B. Chelton, 2008: A global climatology of surface wind and wind stress fields from eight years of QuikSCAT scatterometer data. *J. Phys. Oceanogr.*, **38**, 2379–2413, https://doi.org/10.1175/2008JPO3881.1.

Rouault, M., 2012: Bi-annual intrusion of tropical water in the northern Benguela upwelling. *Geophys. Res. Lett.*, **39**, L12606, https://doi.org/10.1029/2012GL052099.

——, S. Illig, C. Bartholomae, C. J. C. Reason, and A. Bentamy, 2007: Propagation and origin of warm anomalies in the Angola Benguela upwelling system in 2001. *J. Mar. Syst.*, **68**, 473–488, https://doi.org/10.1016/j.jmarsys.2006.11.010.

Rykaczewski, R. R., and D. M. Checkley, 2008: Influence of ocean winds on the pelagic ecosystem in upwelling regions. *Proc. Natl. Acad. Sci. USA*, **105**, 1965–1970, https://doi.org/10.1073/pnas.0711777105.

——, J. P. Dunne, W. J. Sydeman, M. García-Reyes, B. A. Black, and S. J. Bograd, 2015: Poleward displacement of coastal upwelling-favorable winds in the ocean's eastern boundary currents through the 21st century. *Geophys. Res. Lett.*, **42**, 6424–6431, https://doi.org/10.1002/2015GL064694.

Saha, S., and Coauthors, 2010: The NCEP Climate Forecast System Reanalysis. *Bull. Amer. Meteor. Soc.*, **91**, 1015–1058, https://doi.org/10.1175/2010BAMS3001.1.

Samelson, R. M., 1992: Supercritical marine-layer flow along a smoothly varying coastline. *J. Atmos. Sci.*, **49**, 1571–1584, https://doi.org/10.1175/1520-0469(1992)049<1571:SMLFAA>2.0.CO;2.

Seager, R., S. E. Zebiak, and M. A. Cane, 1988: A model of the tropical Pacific sea surface temperature climatology. *J. Geophys. Res.*, **93**, 1265–1280, https://doi.org/10.1029/JC093iC02p01265.

Shaffer, G., O. Pizarro, L. Djurfeldt, S. Salinas, and J. Rutllant, 1997: Circulation and low-frequency variability near the Chile coast: Remotely forced fluctuations during the 1991–92 El Niño. *J. Phys. Oceanogr.*, **27**, 217–235, https://doi.org/10.1175/1520-0485(1997)027<0217:CALFVN>2.0.CO;2.

Shannon, L. V., J. J. Agenbag, and M. E. L. Buys, 1987: Large and mesoscale features of the Angola-Benguela Front. *S. Afr. J. Mar. Sci.*, **5**, 11–34, https://doi.org/10.2989/025776187784522261.

Shchepetkin, A. F., and J. C. McWilliams, 2005: The Regional Ocean Modeling System (ROMS): A split-explicit, free-surface, topography-following coordinates ocean model. *Ocean Modell.*, **9**, 347–404, https://doi.org/10.1016/j.ocemod.2004.08.002.

——, and ——, 2009: Correction and commentary for "Ocean forecasting in terrain-following coordinates: Formulation and skill assessment of the regional ocean modeling system" by Haidvogel et al., *J. Comp. Phys.* 227, pp. 3595–3624. *J. Comput. Phys.*, **228**, 8985–9000, https://doi.org/10.1016/j.jcp.2009.09.002.

Siegfried, L., M. Schmidt, V. Mohrholz, H. Pogrzeba, P. Nardini, M. Böttinger, and G. Scheuermann, 2019: The tropical-subtropical coupling in the southeast Atlantic from the perspective of the northern Benguela upwelling system. *PLOS ONE*, **14**, e0210083, https://doi.org/10.1371/journal.pone.0210083.

Simpson, J. J., 1984: A simple model of the 1982–1983 Californian El Niño. *Geophys. Res. Lett.*, **11**, 237–240, https://doi.org/10.1029/GL011i003p00237.

Skamarock, W. C., and J. B. Klemp, 2008: A time-split nonhydrostatic atmospheric model for weather research and forecasting applications. *J. Comput. Phys.*, **227**, 3465–3485, https://doi.org/10.1016/j.jcp.2007.01.037.

Small, R. J., E. Curchitser, K. Hedstrom, B. Kauffman, and W. G. Large, 2015: The Benguela upwelling system: Quantifying the sensitivity to resolution and coastal wind representation in a global climate model. *J. Climate*, **28**, 9409–9432, https://doi.org/10.1175/JCLI-D-15-0192.1.

Smith, R. D., and Coauthors, 2010: The Parallel Ocean Program (POP) reference manual. Tech. Rep. LAUR-10-01853, 141 pp., https://www2.cesm.ucar.edu/models/cesm1.0/pop2/doc/sci/POPRefManual.pdf.

Strub, P. T., and C. James, 2002: The 1997–1998 oceanic El Niño signal along the southeast and northeast Pacific boundaries—An altimetric view. *Prog. Oceanogr.*, **54**, 439–458, https://doi.org/10.1016/S0079-6611(02)00063-0.

Sverdrup, H., 1947: Wind-driven currents in a baroclinic ocean: With application to the equatorial currents of the eastern Pacific. *Proc. Natl. Acad. Sci. USA*, **33**, 318–326, https://doi.org/10.1073/pnas.33.11.318.

Taboada, F., C. A. Stock, S. M. Griffies, J. Dunne, J. G. John, R. J. Small, and H. Tsujino, 2019: Surface winds from atmospheric reanalysis lead to contrasting oceanic forcing and coastal upwelling patterns. *Ocean Modell.*, **133**, 79–111, https://doi.org/10.1016/j.ocemod.2018.11.003.

Toniazzo, T., 2010: Climate variability in the South-eastern tropical Pacific and its relation with ENSO: A GCM study. *Climate Dyn.*, **34**, 1093–1114, https://doi.org/10.1007/s00382-009-0602-z.

——, and S. Woolnough, 2014: Development of warm SST errors in the southern tropical Atlantic in CMIP5 decadal hindcasts. *Climate Dyn.*, **43**, 2889–2913, https://doi.org/10.1007/s00382-013-1691-2.

——, C. R. Mechoso, L. C. Shaffrey, and J. M. Slingo, 2010: Upper-ocean heat budget and ocean eddy transport in the South-East Pacific in a high-resolution coupled model. *Climate Dyn.*, **35**, 1309–1329, https://doi.org/10.1007/s00382-009-0703-8.

Tsujino, H., and Coauthors, 2018: JRA-55 based surface dataset for driving ocean-sea-ice models (JRA55-do). *Ocean Modell.*, **130**, 79–139, https://doi.org/10.1016/j.ocemod.2018.07.002.

——, and Coauthors, 2020: Evaluation of global ocean-sea-ice model simulations based on the experimental protocols of the Ocean Model Intercomparison Project phase 2 (OMIP2). *Geosci. Model Dev.*, **13**, 3643–3708, https://doi.org/10.5194/gmd-13-3643-2020.

Veitch, J., P. Penven, and F. Shillington, 2010: Modelling equilibrium dynamics of the Benguela Current System. *J. Phys. Oceanogr.*, **40**, 1942–1964, https://doi.org/10.1175/2010JPO4382.1.

Voldoire, A., and Coauthors, 2019: Role of wind stress in driving SST biases in the tropical Atlantic. *Climate Dyn.*, **53**, 3481–3504, https://doi.org/10.1007/s00382-019-04717-0.

Wahl, S., M. Latif, W. Park, and N. Keenlyside, 2011: On the tropical Atlantic SST warm bias in the Kiel climate model. *Climate Dyn.*, **36**, 891–906, https://doi.org/10.1007/s00382-009-0690-9.

Wang, D., T. C. Gouhier, B. A. Menge, and A. R. Ganguly, 2015: Intensification and spatial homogenization of coastal upwelling under climate change. *Nature*, **518**, 390–394, https://doi.org/10.1038/nature14235.

Winant, C. D., C. E. Dorman, C. A. Friehe, and R. C. Beardsley, 1988: The marine layer off Northern California: An example of supercritical channel flow. *J. Atmos. Sci.*, **45**, 3588–3605, https://doi.org/10.1175/1520-0469(1988)045<3588:TMLONC>2.0.CO;2.

Wunsch, C., 2011: The decadal mean ocean circulation and Sverdrup balance. *J. Mar. Res.*, **69**, 417–434, https://elischolar.library.yale.edu/cgi/viewcontent.cgi?article=1309&context=journal_of_marine_research.

Xu, Z., M. Li, C. M. Patricola, and P. Chang, 2014a: Oceanic origin of southeast tropical Atlantic biases. *Climate Dyn.*, **43**, 2915–2930, https://doi.org/10.1007/s00382-013-1901-y.

——, P. Chang, I. Richter, W. Kim, and G. Tang, 2014b: Diagnosing southeast tropical Atlantic SST and ocean circulation biases in the CMIP5 ensemble. *Climate Dyn.*, **43**, 3123–3145, https://doi.org/10.1007/s00382-014-2247-9.

Yeager, S., 2015: Topographic coupling of the Atlantic overturning and gyre circulations. *J. Phys. Oceanogr.*, **45**, 1258–1284, https://doi.org/10.1175/JPO-D-14-0100.1.

Yoshida, K., 1955: Coastal upwelling off the California coast. *Rec. Oceanogr. Works Japan*, **2**, 8–20.

Zemba, J., and C. A. Friehe, 1987: The marine atmospheric boundary layer jet in the Coastal Ocean Dynamics Experiment. *J. Geophys. Res.*, **92**, 1489–1496, https://doi.org/10.1029/JC092iC02p01489.

Zhang, Y., and Coauthors, 2004: Calculation of radiative fluxes from the surface to top of atmosphere based on ISCCP and other global data sets: Refinements of the radiative transfer model and the input data. *J. Geophys. Res.*, **109**, D19105, https://doi.org/10.1029/2003JD004457.

Zuidema, P., and Coauthors, 2016: Challenges and prospects for reducing coupled climate model SST biases in the eastern tropical Atlantic and Pacific Oceans: The U.S. CLIVAR Eastern Tropical Oceans Synthesis Working Group. *Bull. Amer. Meteor. Soc.*, **97**, 2305–2328, https://doi.org/10.1175/BAMS-D-15-00274.1.